KU LEUVEN

FACULTY OF SCIENCE

Asteroseismic picture of the δ Sct star HD 41641 based on CoRoT photometry and HARPS high-resolution spectroscopy

Ana ESCORZA

Promotor: Dr. K. Zwintz
Instituut voor Sterrenkunde
(Katholieke Universiteit Leuven)

Institute for Astro-and Particle Physics
(University of Innsbruck)

Promotor: Prof. C. Aerts
Instituut voor Sterrenkunde
(Katholieke Universiteit Leuven)

Thesis presented in
fulfillment of the requirements
for the degree of Master of Science
in Astronomy and Astrophysics

Academic year 2014-2015

Preface

Stars are the building blocks of our Universe and they represent an important fraction of its visible mass. They control the dynamics of the galaxies through their gravitational interactions. They are also chemical factories that have been enriching the Universe with all elements heavier than lithium since the first generation of stars was born. All these elements have their origin in the fusion processes that take place in the cores of the stars during the main part of their lives. These elements are blown away into the interstellar medium when the stars die, making the formation of new generations of more enriched stars possible. The nuclear fusion also produces huge amounts of energy that are radiated into space. It seems obvious that understanding the structure and evolution of stars is a key issue for astronomy and physics in general.

Powerful instruments have been developed to detect and study the radiation that is received from the stars, covering the whole electromagnetic spectrum. A lot has been learned from the observation of stars, not only about the stars themselves, but also about the evolution, structure and dynamics of galaxies and the Universe. The light of the stars provides us mainly with information originated at their most external layers. How can we probe the stellar interiors? Internal stellar physics and dynamics are a big concern for stellar astrophysicist as it was expressed by Sir Arthur Eddington already in 1926:

> "*At first sight it would seem that the deep interior of the Sun and stars is less accessible to scientific investigation than any other region of the Universe. Our telescopes may probe farther and farther into the depths of space; but how can we ever obtain certain knowledge of that which is hidden behind substantial barriers? What appliance can pierce through the outer layers of a star and test the conditions within?*"

The answer to those questions is closer now thanks to the upswing of *Asteroseismology*. Its refined techniques and the huge improvement in instrumentation and modeling allow nowadays to cross those barriers through the analysis of stellar oscillations. Space data has revolutionized the way of doing stellar science and Asteroseismology is the perfect tool to take advantage of this high quality data. This is thus timely to perform studies like the one that is presented in this master thesis.

All this is possible because most stars pulsate due to the propagation of waves through their interior. The detection and identification of their pulsation frequencies provide the opportunity to probe the inner structure of stars. Oscillating stars have been found all

over the HR Diagram and it is known that a star can present pulsations at most stages of its life. This means that the characterization and interpretation of oscillation modes in different type of pulsators imply an important increase of our knowledge about stellar structure and evolution.

Delta Scuti stars (hereafter δ Sct stars) form one of the first groups of stars that were discovered to pulsate and they still are one of the least understood. Theoretical models cannot completely explain their pulsational behavior. They predict not only less but also different frequencies than those revealed by observations. Asteroseismology, as the bridge between theory and observations, aims to provide new information which allows to put some constraints on the internal structure and choose between different theoretical models. This is why numerous and detailed studies based on observations are important for this type of targets.

Therefore, we want to contribute to the better understanding of stellar structure by analyzing an oscillating star from an asteroseismic point of view. It is a δ Sct star named HD 41641. The scientific questions that we shall address mainly concern this concrete target but they are part of a much wider picture. We would like to finish this report being able to have the answers to several questions about HD 41641 such as (i) which are the frequencies of the oscillations that we observe in this δ Sct star, (ii) are they the same if we study the light curve of the target than if we analyze its spectra, (iii) which are the amplitudes of those oscillations, (iv) which type of waves are propagating through the inner layers of HD 41641, (v) what oscillation modes are excited in this target while many other modes are damped, (vi) is there any other physical effect taking place, apart from oscillations, which might be causing variations with time either in the received light or in the spectral lines, (vi) what physical and chemical information can we derive about the target from the available observations, (vii) does it behave as a typical pure δ Sct star? HD 41641 has not been studied before so this master will contribute to the more general study of δ Sct stars with a wide description of one of their group members.

Summary

This master thesis aimed to draw an asteroseismic picture of a δ Sct star to be a step closer to the understanding of these targets. We tried to extract as much information as we could about this concrete target by studying its photometric and spectral variability. The target, HD 41641, has been simultaneously observed with the CoRoT space telescope and the HARPS high resolution spectrograph installed on the 2.2-meter telescope at ESO-La Silla, Chile. The photometric data set was analyzed with the software package PERIOD04 which, based on classical Fourier Analysis Techniques, allows statistical analyses of large time series. In addition, the software package FAMIAS was used to analyze the line profile variations through the study of the integrated moments of the line profile.

A total of 90 different frequencies was identified and from their analysis it was concluded that the target presents p-mode pulsations with frequencies from 10 to 20 d^{-1}. Combining the results of the photometric frequency analysis with a study of the spectroscopic data set, we suggest the presence of spots on the stellar surface. These spots cause important brightness and line profile variations that are detected in our frequency analysis as a series of harmonics in the low frequency range. Other possible explanations for the signal in the low frequency domain included the combination of frequencies from the p-mode range, g-mode pulsations and binarity. From our analysis, rotational modulation caused by spots are the most probable explanation. We also analyzed the chemical abundances of HD 41641 and found that some peculiar elements vary with the rotation phase. In addition, at least one of the frequencies shows periodic amplitude variability.

Our determination of the fundamental stellar parameters from spectroscopy allows to describe HD 41641 as a moderate rotator ($vsini = 30$ km/s) with an effective temperature of 7200 K and a surface gravity, $logg$, of 3.5 dex. With these values we could investigate HD 41641's position in the HR diagram and hence constrain its mass and its radius. Finally, mode identification was performed with FAMIAS. Although the low frequency peaks that are related to the star's rotation were dominating, some constraints were set on the degree and the azimuthal order of some of the detected modes.

Theoretical modeling is beyond the scope of this master thesis project but, together with a more detailed characterization of the spot nature, these are some of the future prospects to face in light of a possible publication. Also a different approach to the mode

identification might be conducted to try to reduce the influence of the low frequencies and be able to compare our results. This was the first asteroseismic study of the target so no comparison with previous publications was possible.

Summary in Layman′s terms

The interior structure of stars is still an important challenge for astronomers in spite of the effort put on its understanding. The main reason is that the internal layers of stars are not directly observable with our telescopes so indirect techniques are necessary to obtain information about them. The only successful technique that has reached that goal is Asteroseismology, the branch of Astronomy that studies and interprets stellar oscillations.

Most stars can pulsate. They contract and swell as our heart does and this is caused by changes in the physical properties of their interior. These pulsations produce regular changes in the light that we receive from them. The changes are very tiny but can be appreciated and measured with our telescopes and instruments on the Earth and in space. Similar to the study of earthquakes, which provides information about the internal structure of the Earth, the study and interpretation of stellar oscillations allow us to learn about the inner regions of stars and the physical properties that characterize the different layers.

Different oscillating stars present different pulsation patterns and they have been grouped according to this fact. One of those groups is formed by the so-called δ Sct stars. It is one of the first groups of stars that was discovered to pulsate already in the 1930-ies but it still is one of the least understood. Explaining their behavior and why they pulsate in the way they do is still a challenge for astronomers. Complex processes are taking place in the interior of δ Sct stars and not all of them are completely understood. This is what makes it really important to increase the number of studied targets to increase our knowledge about them.

The goal of this master thesis project was studying one of those objects. The pulsational behavior of one δ Sct star has been analyzed using data obtained from space and from the ground. Its name is HD 41641 and nobody had tried to explain its oscillations before. It happened to be an interesting challenge but some important, and previously unknown, information has been derived about it.

List of Figures

List of Tables

Contents

Chapter 1

Scientific framework

1.1 Asteroseismology

Most stars pulsate and their pulsations produce regular changes in their emitted light that our instruments are able to monitor. Asteroseismology uses those stellar oscillations to probe the inner parts of stars. It is the only tool that enables to unravel details of the internal stellar structure which is not directly observable. This is possible through the analysis of the pulsation modes detected in oscillating stars, similar to the study of earthquakes, which allows us to gain knowledge on the interior of the Earth. Each pulsation mode carries different information on the inner structure of the pulsating star.

The physical description of the stellar interior is not a trivial issue. It implies an equation of state, opacity coefficients to evaluate the radiation/matter interaction, nuclear reaction rates appropriate for these physical conditions, a description of all the transport processes at work, boundary conditions defined through a fit to an atmospheric model, etc (see Hansen & Kawaler 1994 and Kippenhahn & Weigert 1990). Huge improvements have been done concerning the description of some of these aspects (e.g. opacity coefficients) but there still is a lack of knowledge about some of the involved physical processes. Asteroseismology provides an important link between theory and observations that implies a potential improvement of these models.

These oscillations that we observe at the stellar surface are caused by waves that propagate inside the star and make it periodically swell and contract. Following the description given by Aerts et al. (2010), it can be compared that, in the same way that the shape of a musical instrument determines which ones of its natural resonant frequencies are excited while others are damped, the internal structure of a star determines which oscillation modes reach its surface. This happens because, in the adiabatic limit, the speed of sound (c) of the gas depends, as defined in Equation (1.1), on the pressure (p) and the density (ρ) and both of them can be related to the temperature (T) and the chemical composition (represented by the mean molecular weight, μ) through an equation of state

like Equation (1.2),

$$c = \sqrt{\frac{\Gamma_1 p}{\rho}}, \tag{1.1}$$

$$p = \frac{\rho k_B T}{\mu m_u}. \tag{1.2}$$

In Equation (1.1), Γ_1 is an adiabatic exponent and in Equation (1.2), the equation of state of an ideal gas, k_B is Boltzmann′s constant and m_u is the atomic mass unit.

These equations help to understand that, if we were able to measure the speed of sound throughout a star, we would have information about the density and temperature structure of its interior and hence, reduce the number of uncertainties that stellar models have to deal with. Asteroseismology uses observations to extract the frequencies, amplitudes and phases of the waves that reach the surface and those numbers can be used to determine the sound speed inside a star. As different modes penetrate to different depths, the more modes that are detected and analyzed, the more detailed the internal structure map will be.

Sound waves were used here to make the goal of Asteroseismology clear but not every wave that propagates throughout the stellar interior is an acoustic wave. Pulsation is characterized by the nature of the restoring force that is responsible for the oscillatory behavior. For acoustic (p-) modes, the pressure force is the dominant restoring force. Such modes can be found in the Sun and in many types of pulsating stars, e.g in δ Sct stars. Gravity (g-) modes, for which the dominant restoring force is buoyancy, can, for example, be found in γ Dor stars and white dwarf pulsators (Aerts et al. 2010, Chapter 2). The g-modes are more sensitive to the conditions in the deep interior so their detection provides information of the most inner layers while p-modes probe the outer layers of the stars.

Difficulties remain sometimes to reconcile theory and observations. This means that something is being either misunderstood or not correctly taken into account in the modeling. For this reason, it is very important that observational astronomy deeply analyzes as many targets as possible to keep providing stellar models with new input information. It is important to be aware of the fact that detecting these oscillations was not an easy issue not so many years ago when it had to be based on observations taken with ground-based telescopes. This is different now since space missions such as CoRoT (Auvergne et al., 2009) and Kepler (Koch et al., 2010) revolutionized this branch of astronomy. Figure 1.1 presents, as an example, a section of a Kepler light curve of a δ Sct star and its Fourier spectra to show the high quality of space data.

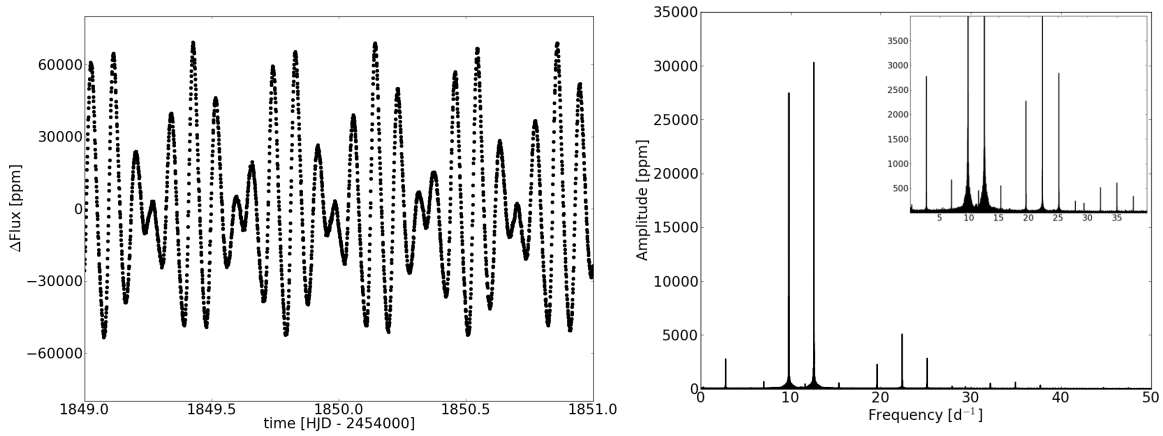

(a) (b)

Figure 1.1: Example of a Kepler Light curve of the δ Sct star KIC 9700322 studied by Breger et al. (2011) and its Fourier spectrum.

1.1.1 Oscillation modes

A star is a three dimensional gaseous pulsator. It is useful to think about it as the 3D analogue of the one-dimensional oscillations of an organ pipe. Stellar oscillation modes have nodes in three orthogonal directions and are described by their distance (r) to the center of the star, their co-latitude (θ) measured from the pulsation pole and their longitude (ϕ). Assuming spherical symmetry, the solutions to the equations of motion are given by Equations (1.3), (1.4) and (1.5),

$$\xi_r(r,\theta,\phi,t) = a(r)Y_l^m(\theta,\phi)\exp(-i2\pi\nu t), \tag{1.3}$$

$$\xi_\theta(r,\theta,\phi,t) = b(r)\frac{\partial Y_l^m(\theta,\phi)}{\partial\theta}\exp(-i2\pi\nu t), \tag{1.4}$$

$$\xi_\phi(r,\theta,\phi,t) = \frac{b(r)}{sin\theta}\frac{\partial Y_l^m(\theta,\phi)}{\partial\phi}\exp(-i2\pi\nu t), \tag{1.5}$$

where ξ_r ξ_θ and ξ_ϕ are the displacements, a(r) and b(r) are amplitudes, ν is the oscillation frequency and $Y_l^m(\theta,\phi)$ are spherical harmonics given by Equation (1.6),

$$Y_l^m(\theta,\phi) = (-1)^m\sqrt{\frac{2l+1}{4\pi}\frac{(l-m)!}{(l+m)!}}P_l^m(cos\theta)\exp(im\phi), \tag{1.6}$$

where $P_l^m(cos\theta)$ are Legendre polynomials given by Equation (1.7),

$$P_l^m(cos\theta) = \frac{1}{2^l l!}(1 - cos^2\theta)^{m/2}\frac{d^{l+m}}{dcos^{l+m}\theta}(cos^2\theta - 1)^l. \tag{1.7}$$

More information about the properties of the Legendre functions and the spherical harmonics can be found in Appendix B of Aerts et al. (2010).

Hence, there are three quantum numbers that are necessary to completely describe an oscillation mode:

- n, related to the number of radial nodes and called the overtone of the mode;
- l, the degree of the mode which specifies the number of surface nodes;
- m, the azimuthal order that ranges from -l to +l and whose absolute value specifies how many of the surface nodes are lines of longitude. By convention, a positive m means that the wave is traveling in the direction of stellar rotation (prograde modes) while waves with negative m are traveling against rotation (retrograde modes).

Modes with l = 0 are called radial modes. The fundamental radial mode ($n = 0$) makes the star contract and swell, heat and cool, with the core as a node and the surface as a displacement antinode (as in an organ pipe, one of the extremes is closed and fixed while the other one is open). The first overtone radial mode ($n = 1$) has one radial node, a concentric shell within the star that does not move while motions above and below it are in antiphase.

In an organ pipe, where the sound speed is constant, the ratio of the first overtone period to the fundamental period is 0.33. There are stars that pulsate simultaneously in the fundamental and first overtone radial modes and for which this ratio has been observed to be very different. For example, for δ Sct stars, it is know to be about 0.77 (firstly studied by Petersen 1973 and Petersen 1978). This provides direct evidence of a sound speed gradient, hence of temperature and chemical composition gradients inside the stars. This is mathematically described by the pulsation constant Q (Equation 1.8) which describes the period-density relation,

$$Q \equiv P\sqrt{\frac{\rho}{\rho_\odot}}, \tag{1.8}$$

where P is the pulsation period and ρ and $\rho_\odot$ are the mean density of the star and the Sun respectively.

There are also nonradial modes. The simplest one is the axisymmetric dipole mode with $l = 1$ and $m = 0$ for which the equator is a node and the northern hemisphere swells up while the southern hemisphere contracts and vice versa. Nonradial modes only occur for $n \geqslant 1$, so in the case of the $l = 1$ dipole mode, there is at least one radial node within the star.Modes with two surface nodes ($l = 2$) are known as quadrupole modes, those with three surface nodes ($l = 3$) are called octupoles, etc. Figure 1.2 represents a set of octupole modes to help creating a mental picture of how the stellar surface behaves. The modes are observed from three different inclination angles with respect to our line-of-sight.

Observation of oscillation modes

Unfortunately, we cannot resolve stellar surfaces and detect the nodal lines directly (it can only be done for the Sun due to its proximity). Hence, we have to deal with observations representing integrated quantities over the surface of the star. For high degree l, the surface is divided in more sectors and their contributions tend to cancel out in photometry. The effect is called *partial cancellation* and implies that low-degree modes are easier to detect. This is a consequence of geometry and the total number of nodal lines on the stellar surface. This partial cancellation effect is different for spectroscopic time series where the detectability of modes does not decrease for modes with higher degree. In this case, p-modes with the same intrinsic amplitude are easier to detect when they are of degree $l = 1$ or 4 than when they are of $l = 2$ or 3 and g-modes are always more difficult to detect than p-modes (Aerts et al., 2010).

Another important geometrical effect that observational astronomers have to deal with is related to the orientation of the stellar rotation axis and the inclination angle (i) between this axis and the observer line of sight. The observed amplitude of an oscillating mode strongly depends on this angle and for every mode, there exists at least one inclination angle that causes so-called *complete cancellation*. This occurs when the star is being observed in such a way that the contribution to the brightness of an element of the stellar disk exactly cancels out the contribution of another one. As a consequence, no brightness variation is detected in time, as if that mode was not excited at all.

It is also important to mention the effect of rotation. For an ideal, non-rotating, spherically symmetric star, the 2l+1 frequency members of a multiplet would have the same value. Deviations from this ideal situation lead to frequency degeneracy. Stellar rotation is an important physical cause of departure from spherical symmetry and causes pulsational variations that make prograde modes have frequencies slightly lower than the m = 0 mode and retrograde modes have slightly higher frequencies. Moreover, in a real star, rotation is not expected to be uniform so the rotational splitting is more complicated than that. Components of the same multiplet can be excited to different amplitudes and some of them may be absent strongly hindering their interpretation. The positive aspect is that when such rotationally split multiplets of modes of different degree or different

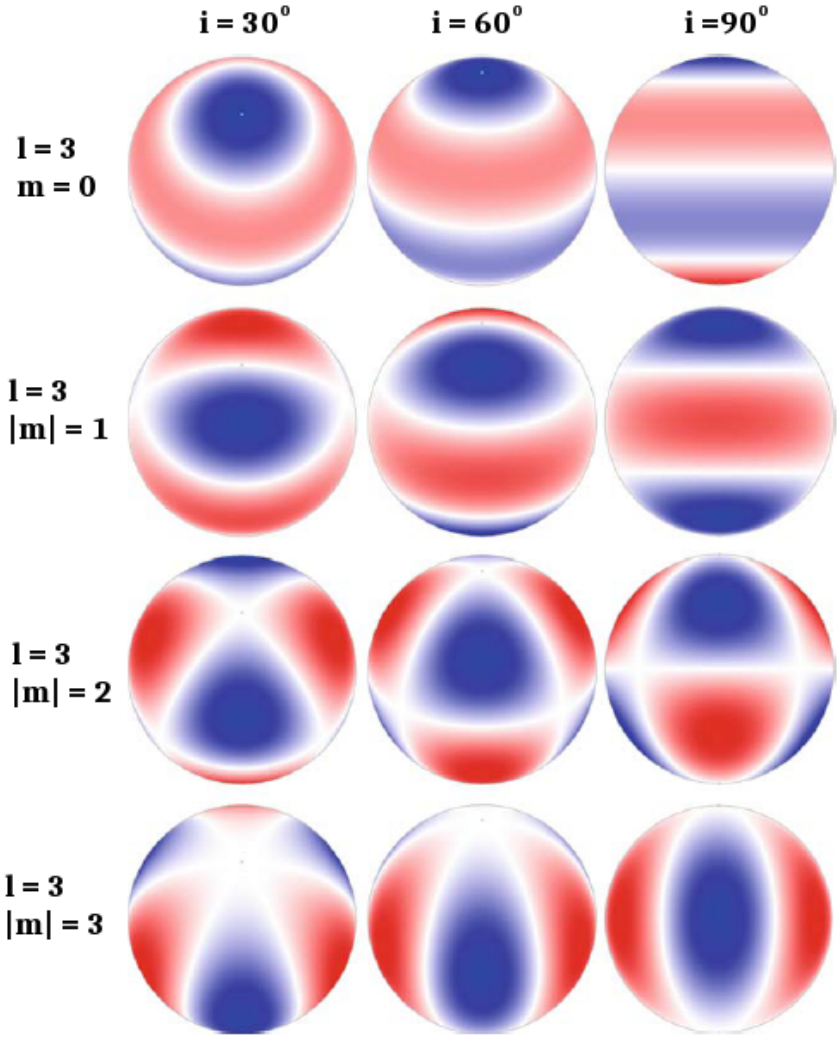

Figure 1.2: Snapshot of the radial component of the l = 3 octupole modes at different inclination angles. The white bands are the surface nodes and the red and blue section move in antiphase. Figure from Aerts et al. (2010).

overtone are observed and identified in the same star, information about the interior rotation rate can be derived and this is very important because it is not knowable by any other means, see Kurtz et al. (2014) and Saio et al. (2015).

In most pulsating stars the pulsation axis coincides with the rotation axis but there are more complicated situations such as in rapidly oscillating Ap stars, where the axis of pulsational symmetry is the magnetic axis that is inclined with respect to the rotational axis (Kurtz, 1992).

Mode identification

We described several complications when identifying the oscillation modes that give rise to each detected frequency but this is a crucial step to reach successful seismic modeling. Going back to the example of a pressure wave, the determination of a frequency gives information about the sound travel time along its path but to know the sound speed, it is necessary to know the path itself, and this is given by the geometry of the mode. The precise determination of the pulsational frequencies and the identification of the quantum numbers l and m of each one of them is a necessary step before asteroseismic modeling can be done. Several methods have been developed to achieve such mode identification.

Mode identification can be performed based on photometric measurements in different filters. This happens because the temperature variations related to the pulsations are wavelength dependent so the amplitude of a mode observed in different filters is as well. In addition, the dependence of the pulsation amplitude with the wavelength is affected by the geometry of the mode so, if a certain frequency is detected with several filters, the comparison of its detected amplitudes gives information about the degree l (m cannot be determined with this method). Further information and references can be found in Chapter 6 of Aerts et al. (2010).

The second diagnostic for mode identification is the analysis of line profile variations from time series of high-resolution spectroscopy. Spectroscopy also allows the determination of the azimuthal order m and it is in fact the only known tool to determine both quantum numbers simultaneously (Zima et al., 2007). Moreover, it can also set constraints to the stellar inclination. Several different methods have been developed to perform mode identification based on spectroscopy: the moment method (Aerts, 1996), the intensity-period-search method (Schrijvers et al., 1997), the pixel-by-pixel method (Mantegazza, 2000) and the Fourier parameter fit method (Zima, 2006). The moment method fits integrated values across the profile with theoretical values. These are the moments of the spectral line and can be described by Equation (1.9),

$$\langle v^n \rangle_I (t) = \frac{\int_{-\infty}^{\infty} v^n I(v,t) dv}{\int_{-\infty}^{\infty} I(v,t) dv}, \tag{1.9}$$

where the zeroth moment is the equivalent width (EW); the first moment is connected with the radial velocity (RV); the second moment with the variance and the third one with the skewness. The other three methods have a common approach and rely on the Doppler broadening of the line profiles.

To be able to detect and analyze line profile variations, some requirements are sufficiently high resolving power ($> 40\,000$) and signal-to-noise ratio (> 200) combined with a good time coverage that will lead to a good temporal resolution (below a few per cent)

(Aerts et al., 2010). The effort invested in the last decades in the improvement of spectrographs and their temperature stable environment is what has made these requirements to have become reachable.

1.1.2 Driving mechanisms

As a star pulsates it contracts and swells, heats and cools, so mechanical energy is captured in every pulsation cycle when the oscillations are not damped. This means that, if pulsations are a stable phenomenon, there have to be a mechanism that feeds the pulsations with enough energy to overcome the damping. These are the so-called driving mechanisms and they are the reason why the different modes become detectable.

Most of the classical pulsating stars exhibit self-excited modes, i.e. one layer of the stars acts as a heat-engine driving the pulsation. This effect is known as the opacity (κ-) mechanism and is connected to the opacity of the most abundant elements such as Hydrogen or Helium or to elements with a very rich atomic structure such as Iron. To understand how it works, let us consider a layer of the star that starts moving inwards. Pressure is higher at the inner parts so, due to its movement inwards, this layer compresses and let us assume that the opacity increases. Then the radiation that is coming from the core is blocked and unable to escape through that layer. The consequence of this is that the gas is heated up, the pressure increases, the gas swells and the layer starts an outwards motion. The layer will expand, cool down, and become less opaque to radiation again so the energy trapped can be released. This makes the pressure drop and the layer starts falling inwards again restarting the cycle. Therefore the opacity mechanism is considered to be an analogue to a heat engine.

In the previous description, opacity was considered to increase with compression but according to Kramers opacity law (Equation 1.10) this is not true in most stellar layers,

$$\kappa \propto \rho T^{-7/2}, \tag{1.10}$$

where κ is opacity and ρ and T are the local density and temperature of the medium. It can be deduced from Equation (1.10) that the opacity is more sensitive to the temperature than to the density so, as the layer of the star is compressed and both density and temperature rise, the opacity will decrease. This means that for this pulsation mechanism to work, special conditions are needed and those are found to occur in partial ionization zones. In these special regions, part of the energy that would normally make the temperature rise during compression is used to ionize the medium. The consequence is that the temperature does not increase substantially but the opacity increases due to the higher density.

One more requirement for modes to be excited by the κ-mechanism is that the local thermal timescale (τ_{th}) in the driving zone must be comparable or longer than the oscillation period. This time scale is given by,

$$\tau_{th} \equiv \int_r^R T c_P \frac{dm}{L} \tag{1.11}$$

where T and L are the temperature and the luminosity of the considered layer (from a given r to R), c_P is the heat capacity of the gas at constant pressure and dm the mass content in the layer. If this values is shorter than the oscillation period, the medium have enough time to recover thermal equilibrium and the mode is not excited. As seen from Equation (1.11), the local thermal time scale depends on local stellar parameters so the excitation of a mode with a given period will depend on the depth of the partial ionization zone that is causing the opacity bump.

The second important mechanism is stochastic excitation and drives oscillations in the Sun, solar-like oscillators and red giants. These stars all have an outer convection zone where the turbulent convective motions can reach speeds close to the sound speed. This is an efficient source of acoustic energy that can make the star resonate in some of its natural oscillation frequencies. Oscillation modes that are damped can still be driven to observable amplitudes due to these re-occurring turbulent convective motions.

Because of the large number of convective cells moving up and down, the excitation is random rather than coherent. This mechanism can excite modes in a broad range of frequencies to observable amplitudes and they appear with a characteristic amplitude distribution that simplifies mode identification by pattern recognition. This is very different from mode excitation by the κ-mechanism where the amplitudes cannot be predicted. The driving of stochastic modes is not related to the depth of the driving layer as it was for the opacity mechanism but rather to the efficiency of convection which is one of the most difficult phenomena to describe in stellar astrophysics.

One last driving mechanism which will just be mentioned is the so-called ϵ-mechanism where the ϵ refers to the energy generation rate in the core of the star. Variations in this rate have been discussed to be able to drive pulsations in some evolved very massive stars, but there is no known star where pulsations are proven to be driven by the ϵ mechanism alone.

1.1.3 Oscillating stars

Figure 1.3 (Papics, 2013) represents a pulsation Hertzsprung-Russell (HR) diagram showing different classes of oscillating stars. In the plot, the color reflects the spectral type of

the stars and the filling pattern indicates the dominant pulsation type where // means that g-modes dominate and \\ indicates that p-modes do. The plot includes evolutionary tracks for different stellar masses (solid black lines), the limits of the classical instability strip (dark grey dashed lines) and the zero-age main sequence (lighter dashed line).

From the figure it can be observed that oscillating stars can be found all over the HR diagram and that stars can become pulsationally unstable during almost every stage of stellar evolution. Different instability regions appear depending on the dominant driving mechanism and the type of exited modes, both of which are very sensitive to the detailed

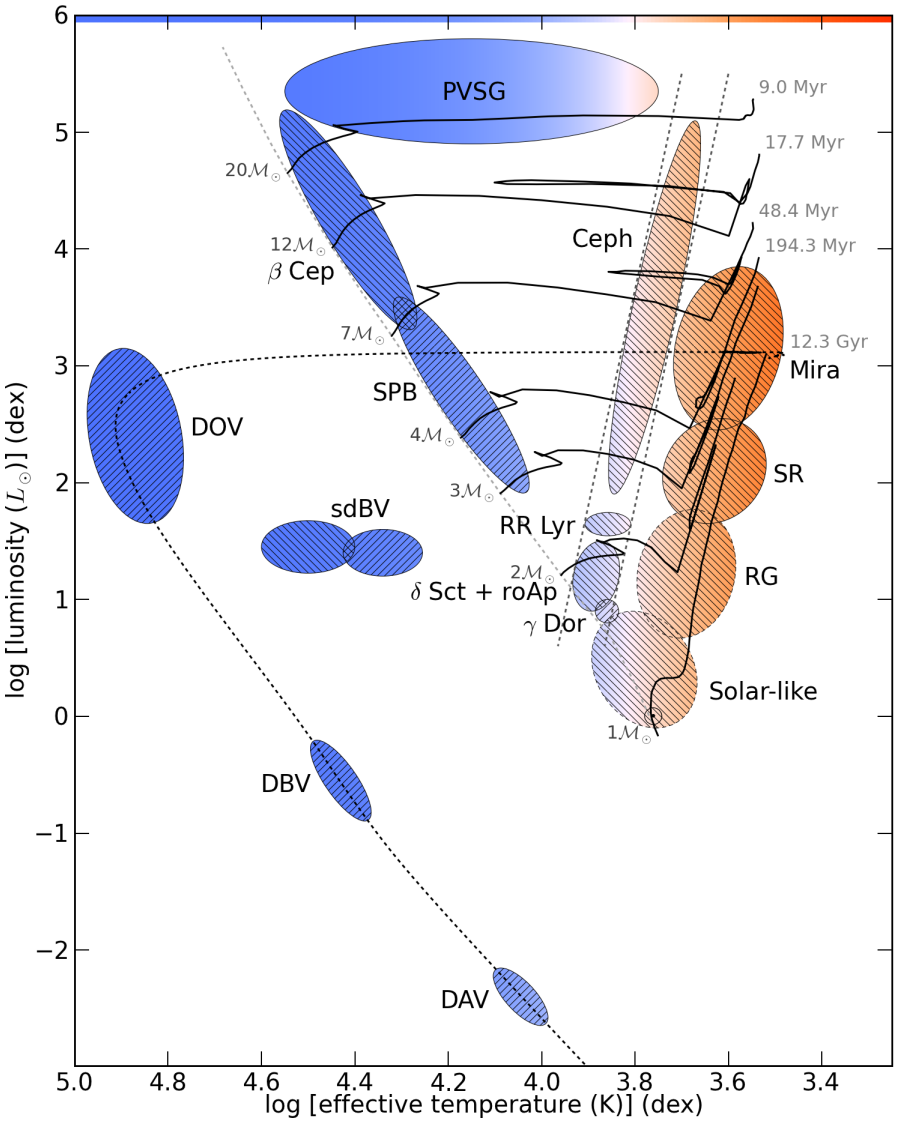

Figure 1.3: Different pulsating stars present in the HR diagram (Papics, 2013)

physical properties of the star.

There is a region in which oscillations are much more apparent and it is called the *classical instability strip*. The detected pressure modes in the stars that are found in this region (i.e. Cepheids, RR Lyrae stars, δ Sct stars and rapidly oscillating Ap) are primarily driven by the previously explained κ-mechanism acting in the second partial ionization zone of Helium. This is also the case of pre-main-sequence pulsators. The κ-mechanism is also the dominant exciting mechanism of the g-modes detected in slowly pulsating B stars (SPB) and the p-modes observed in β Cephei pulsators but, in these cases, it is acting in partial ionization zones of elements of the iron group. The same mechanism is responsible for the oscillations in subdwarf B (sdB) stars, while the excitation mechanism of Periodically Variable B Supergiants remains unclear.

To the right of the cool (red) edge of the *classical instability strip*, cool red giants and supergiants (Mira stars), semiregular variables (SR) and solar-like and giant solar-like oscillators are found. The presence of a convective region reaching the surface sometimes combined with the κ-mechanism acting in the first partial ionization zones of Hydrogen and Helium drives the pressure modes observed in these stars. The presence of convective surface layers also contributes to the driving of gravity modes in variable white dwarfs of spectral type A, B and O (DAV, DBV and DOV).

Finally, in Figure 1.3, γ Doradus stars can be found very close to the intersection between the *classical instability strip* and the main sequence. These pulsators present gravity modes excited by a convection-related mechanism that causes flux blocking at the bottom of their convective envelope. It can be observed that the γ Dor instability region (g-modes) slightly overlaps the δ Sct and the solar-like oscillator regions (p-modes). There are two more regions where p-mode and g-mode pulsators of similar stellar structure are present: one on the upper main sequence where β Cep (p-modes) and SPB (g-modes) regions overlap and another one concerning sdB variables. Stars pulsating in both p modes and g modes simultaneously (known as hybrid pulsators) are of particular interest as they present the most complete view of their interior. KIC 11145123 (Kurtz et al., 2014) and KIC 9244992 (Saio et al., 2015) are interesting examples of pulsators for which the simultaneous detection of both types of modes led to the successful determination of surface-to-core rotation rates from rotational splitting of pressure and gravity modes.

1.2 δ Sct Stars

The target of this work (HD 41641) is a δ Sct star. As it was seen in Figure 1.3, the δ Sct instability region is situated in the lower part of the *classical instability strip* where it intersects the main sequence. Hence, δ Sct stars either are in their core hydrogen-burning phase or they have recently evolved towards the phase of shell hydrogen burning. Recently

some δ Sct variables have also been identified to be in their pre-main-sequence stage, e.g. Zwintz et al. (2011).

The blue edge of the δ Sct instability strip has been theoretically determined based on the study of the excitation mechanism and the helium opacity bump, e.g., Pamyatnykh (2000). The red edge is a more complicated issue. For the coolest δ Sct stars, the heat-mechanism is no longer efficient enough and the driving of modes is strongly influenced by convection, making their modeling much more difficult (see Dupret et al. (2005)).

The δ Sct stars are of spectral types A and F. Their masses are in the range between 1.5 $M_\odot$ and 4.0 $M_\odot$ and their pulsation periods range from about 20 minutes to 0.3 days. They are usually multiperiodic and present both radial and nonradial p-modes, generally of low degree l. The amplitudes of those cover a wide range between several millimagnitudes and a few micromagnitudes, which translates to a range of several to several thousands ppm (parts-per-million) in flux. The κ mechanism acting in the second ionization zone of Helium is responsible of their pulsational behavior.

A/F-type stars in general represent interesting targets to improve our understanding of stellar structure and evolution. An important fraction of A/F-type stars are relatively fast rotators and their rapid rotation influences their structure. A subsample known as Ap stars are slow rotators but show strong magnetic fields and remarkable chemical peculiarities. These magnetic fields can lead to a non-uniform distribution of chemical elements on the stellar surface, including the formation of chemical spots (Kochukhov, 2011).

In addition, δ Sct stars are intermediate-mass stars situated just above the main sequence and because of their mass range, they are known to have convective cores during their main sequence phase. That means that convection-related aspects as the mixing beyond the convective core and turbulent motions in the envelope may have important effects on their structure and evolution. These effects complicate the theoretical modeling. For a detailed introduction into the theoretical aspects of δ Sct stars see Christensen-Dalsgaard (2000). From an asteroseismic point of view, they also are particularly useful as they present a large number of simultaneously excited independent pulsation modes and every single identified pulsation frequency provides information that potentially allows to distinguish between different theoretical models.

There are some very well studied δ Sct stars, such as FG Vir (Breger et al., 2009) and 4 CVn (Schmid et al., 2012) which have been targets of extensive photometric and spectroscopic observation campaigns. Despite of the efforts, no definite model has been achieved for them yet: δ Sct stars are one of the first known groups of pulsators and still one of the least understood.

Before the era of space photometry, theoretical models used to predict a factor ten more unstable modes than observations revealed but, after having studied δ Sct stars

with the CoRoT (Auvergne et al., 2009) and Kepler (Koch et al., 2010) space missions, the opposite seems to be the case. It was already mentioned that space photometry was an almost essential requirement to perform asteroseismology but it has been particularly revealing in the case of δ Sct stars. Several hundreds of frequencies have been detected for some targets studied from space data (e.g. Poretti et al. (2009), Balona & Dziembowski (2011)) revealing much more frequencies than models predict. The number of detected frequencies for δ Sct stars strongly increases with decreasing amplitude. Hence, with time series photometry from space the detection threshold shifted towards lower amplitudes and the number of detectable frequencies increased significantly.

There is another known problem for δ Sct stars. Some of the theoretically expected frequencies are not detected observationally while other frequencies that are not predicted by the models are discovered from observations. In addition, different targets challenge the theory in different aspects. As an example, the detection of frequency spacings in the Fourier spectrum are not generally expected for δ Sct stars but a few of them have presented some evidences of periodic structures, e.g. García Hernández et al. (2009), García Hernández et al. (2013) and Mantegazza et al. (2012).

Another challenging target is HD 187547, which initially looked like a typical δ Sct star but, at high frequencies, Antoci et al. (2011) detected modes approximately equidistantly spaced, as expected for high radial order p-modes, which are not combination frequencies. As the κ mechanism cannot excite a continuous frequency region as observed and the spectroscopic observations exclude binarity, Antoci et al. (2011) suggest that convection dynamics are playing a role as a exciting mechanism. However, this result could not be confirmed by additional data (Antoci et al., 2014).

The list of observational exceptional seismic behavior is long for δ Sct stars and these existing problems when trying to reconcile theory and observations tell us that shortcomings in our theoretical picture of δ Sct stars occur. This is our motivation to keep providing new observational constraints for this type of stars through studies like the one presented here.

1.3 HD 41641

The goal of the project was to conduct a detailed study of the δ Sct star HD 41641 and we focused on the analysis of its pulsational behavior. The identification and analysis of its oscillation frequencies and the identification of the excited oscillation modes were our main goals. This master thesis was based on CoRoT (Auvergne et al., 2009) space photometry and high-resolution spectroscopy from HARPS (Lovis et al., 2006) and it is the first asteroseismic study of this target. Apart from the general information found in the SIMBAD database (Wenger et al., 2000), i.e. coordinates, spectral type and magnitudes

Table 1.1: Summary of the information about HD 41641 found in the literature. The references are: (1) van Leeuwen (2007), (2) Grenier et al. (1999), (3) Høg et al. (2000), (4) Gontcharov (2006) and (5) Poretti et al. (2005).

α_{2000}	$06^h06^m40.578^s$ (1)
β_{2000}	$+06^o43'49.886"$ (1)
Spectral type	A5III (2)
V_{mag}	7.86 ± 0.01 (3)
Radial Velocity	28.60 ± 2.50 km/s (4)
Effective temperature	7700 ± 200 K (5)
Surface gravity	3.9 ± 0.2 dex (5)
Metallicity [M/H]	-0.2 ± 0.2 dex (5)
Projected rotational velocity	29 ± a few km/s (5)

at different wavelengths, only Poretti et al. (2005) provide some extra information about the target. The stellar fundamental parameters of HD 41641 were derived from photometric observations together with the fundamental parameters of several other CoRoT candidate targets. All the target information found in the literature is summarized in Table 1.1.

Chapter 2

CoRoT space photometry

2.1 The CoRoT mission

In the nineties, it had been shown (e.g. Gilliland 1995) that the limitations of ground-based photomety were too restrictive to perform asteroseismology and exoplanet science. The necessity to go to space was an evidence as the required precision and duty cycle were impossible to be achieved from the ground. Indeed, it was known to be difficult to obtain a good time coverage from Earth even if a large network of telescopes was built. The day-night cycle and the climate caused unavoidable temporal interruptions that would not be a problem anymore from space. The Earth atmosphere was also a well-known limitation to achieve the needed precision that would vanish if we put our instruments in orbit.

The Canadian micro-satellite MOST (Microvariability and Oscillations of STars) had already shown the opportunities that space photometry offered even with a small satellite (Walker et al., 2003). The increase of the number of detectable frequencies, particularly for δ Sct pulsators (Matthews, 2007), had made scientists conclude that space photometry could probably surpass the highest quality data obtainable from the ground, especially as far as duty cycle is concerned. Within this context, the CoRoT mission was developed.

CoRoT (COnvection, ROtation et Transits planétaires) is a space telescope that was launched on December 27, 2006 into a low Earth polar orbit at an altitude of 896 km (Auvergne et al., 2009). The mission was led by the Centre National d'Études Spatiales (CNES) in collaboration with the European Space Agency (ESA) and seven other international partners, among which Belgium. The satellite carries a 27cm-diameter telescope equipped with a four-CCD camera which provided continuous and very long observations of the same stellar field. These fields consisted of two cones of 10° of diameter centered at right ascensions α = 18h50m and α = 6h50m which are sometimes referred to as the "CoRoT eyes". The telescope used to spend about five months per year observing in one direction and five months in the opposite one depending on the position of the Sun. CoRoT is not operational since a hardware failure in November 2012.

The role of CoRoT was to measure relative brightness variations over time of its target stars to a very high precision. This made it a pioneering mission in stellar seismology and studies of exoplanets, the two scientific goals of the mission. The requirements of the two programs were slightly different so two different types of runs, "long" ($\sim$ 150 days) and "short" ($\sim$ 30 days), were planned to cover the necessities of both types of observations. In this way, small planets with long orbital periods could be studied with the same telescope that was also designed to observe oscillating stars covering the whole HR diagram (Boisnard & Auvergne, 2006).

In the course of the CoRoT mission, nearly 160,000 light curves were obtained with a very high precision. These have allowed the detection of more than 500 transiting exoplanet candidates and the discovery and interpretation of oscillations in numerous stars. CoRoT has also helped to address several other questions in astronomy such as, for example, stellar activity, early stellar evolution, stellar rotation or binarity.

In the particular case of asteroseismology, CoRoT opened new opportunities to our general understanding of stellar structure and had several breakthrough contributions to stellar astrophysics. For example, it provided us with the first unambiguous photometric detection of solar-like oscillations outside the solar system. The mission also revealed that some oscillating stars could vibrate with several hundreds of frequencies as it is the case of some δ Sct stars (see Poretti et al. 2009; García Hernández et al. 2009 or Mantegazza et al. 2012) while from the ground, only a few tens of those frequencies had been observed. This increase of the number of detectable frequencies has been crucial for the improvement of stellar modeling.

2.2 Observations and data reduction

The received data at the CoRoT Data Center is processed to two different levels. The raw data, called N0 data, is corrected from instrumental effects to produce N1 data which is corrected again in a second step. The final product, called N2 data, consists of the target light curves ready for scientific usage without the necessity of any additional reduction procedure (Baudin et al., 2006). These light curves are now publicly available at their science archive[1] .

HD 41641 was observed by CoRoT during 94 continuous days from December 17, 2010 to March 22, 2011 during the run named LRa05. It was one of the five targets of the asteroseismology channel for this run. Initially, the photometric N2 data set consisted of 254 978 measurements of detected flux in electrons per second. The exposure time for the

[1] http://idoc-corot.ias.u-psud.fr/

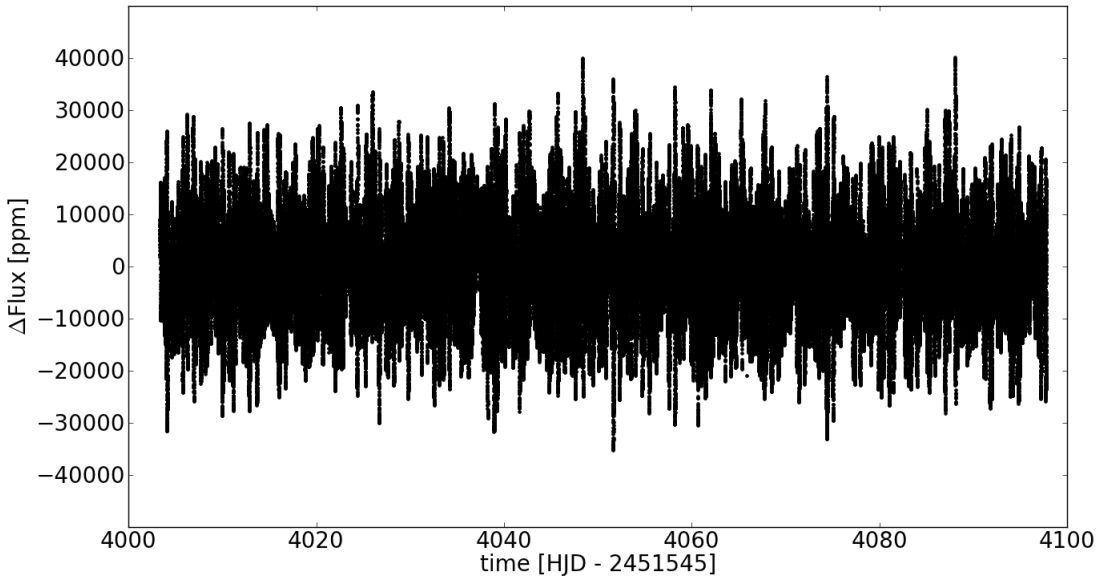

Figure 2.1: Complete CoRoT light curve of HD 41641.

seismology program is 32 seconds in the satellite reference frame and the final flux value is given as the sum of all 1-second exposures divided by the number of valid ones. Each flux point is associated to the time of the observation expressed in Heliocentric Julian Days [HJD] minus a constant that corresponds to the CoRoT zero-point in time, chosen as the 1st of January, 2000 at 12:00 (HJD 2451545.0). The sampling is regular in the satellite reference frame but, when the time points are translated to the heliocentric reference frame, the result is a slightly non-equidistant sampling with an average exposure time of 32 seconds.

Attached to each flux value, the data set also includes an uncertainty, the standard deviation of the measurements at one second, and a status flag. Each point had been labeled with a "0" when it was a valid flux measurement and could have several different bad-status flags depending on the reason why it was not valid. About 12.5% of our observations had been flagged as invalid and were removed from the data set. Most of them were interpolated estimates of the flux. The reason why these points needed to be interpolated varied but the most common reason was that the flux was acquired when the satellite was crossing the South Atlantic Anomaly (SAA)[2], entering the Earth penumbra or entering light. This implied a duty cycle of 87.5% and a final light curve of 223 146 flux points that is shown in Figure 2.1. The two panels of Figure 2.2 are a 6-day subset and a 2.5-day subset showing the complicated oscillation patterns that the light curve

[2]It is a region where the Van Allen radiation belts (rings of charged particles) come closest to the surface of the Earth due to a local minimum in the geomagnetic field. Satellites and their instruments can be seriously damaged when cross it because of the increased flux of energetic particles.

Table 2.1: Summary of the characteristics of the CoRoT photometric data set

CoRoT run	Valid data points	Duty cycle	Total length	Frequency resolution	Nyquist frequency
LRa05	223 146	87.5%	94 days	~ 0.01059 d^{-1}	1320.91 d^{-1}

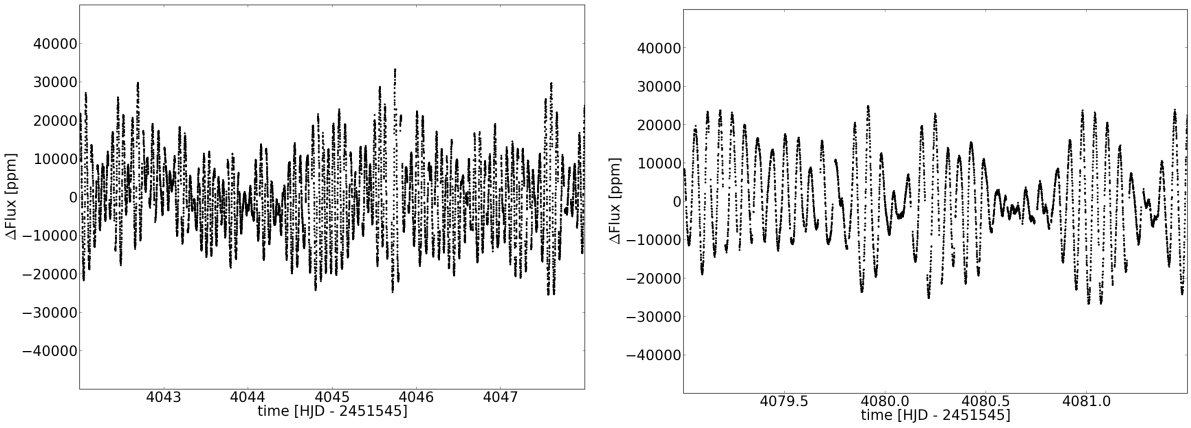

(a) (b)

Figure 2.2: Two subsets of the CoRoT light curve of HD 41641.

presents and Table 2.1 summarizes the characteristics of the data set, i.e. the name of the run during which it was obtained, the number of valid points, the duty cycle, the total length of the data set, T, the frequency resolution (1/T) that it implies and the Nyquist frequency which will be explained in the next section.

2.3 Frequency analysis

2.3.1 Extraction of oscillation frequencies

The software package Period04 (Lenz & Breger, 2005), which is based on classical Fourier Analysis Techniques, was used to identify the oscillation frequencies of HD 41641. A harmonic model function is fitted to the data assuming that the light curve can be described as a combination of sinusoidal functions. Period04 allows statistical analyses of large time series and the extraction of individual frequencies by analyzing the frequency spectrum of the data set.

In the case of photometric data, the light curve is studied in Fourier space and its spectrum will be observed to present several peaks at frequencies of detected periodici-

ties. The highest peak will be considered to appear at the first significant frequency. Once a frequency, F_i, is identified, its contribution to the light curve is estimated by performing a least-squares fitting procedure using the sine function $f(t)$ described by Equation (2.1):

$$f(t) = Z + \sum A_i sin(2\pi(F_i t + \Phi_i)), \tag{2.1}$$

where Z is a constant, A_i, the amplitude of the oscillation, Φ_i the phase and t the time.

Then, the best fitting sinusoidal model is pre-whitened from the original data and the procedure is repeated. Now, the second significant frequency is searched as the highest peak in the Fourier spectrum of the residual light curve, after having removed the contribution of the already found frequency.

The Nyquist frequency (f_{Ny}) is a mathematical limit that corresponds to half the inverse of the sampling rate in the case of evenly spaced data and above which, the search of intrinsic oscillation frequencies has to be treated with caution. According to Period04, the Nyquist frequency of our data set was 1320.91 d^{-1} (see Table 2.1) which is close to the expected one (1350 d^{-1}) if the measurements had been regularly taken every 32 seconds and there were no gaps among them. As it was stated in the introduction, a δ Sct star is expected to oscillate with frequencies in a range between 3 d^{-1} and about 75 d^{-1} so an upper limit of 100 d^{-1} was selected to do the analysis, rather than the whole range up to the Nyquist frequency. The procedure was performed once over the whole range up until the Nyquist frequency to support this decision and no statistically significant peak was found outside the selected range above 100d^{-1}.

The left panel of Figure 2.3 shows the spectral window of the light curve and the right panel shows the region of the Fourier spectrum where peaks could be observed. Note that no significant intrinsic signal was found in the region from 40 to 100 d^{-1}. Most of the peaks appear over the threshold of a few d^{-1} and will probably be caused by the excitation of pressure modes but there are also several peaks at lower frequencies that correspond to the gravity mode region.

The spectral window corresponds to the Fourier spectrum that the data would have if all the measurements were of equal flux. Hence, it shows peaks at frequencies that are not intrinsic to the target but relate to noise, instrumental effects, the time of observations, gaps in the data... Comparing its behavior with the Fourier spectrum of the data will help to conclude if a detected frequency is caused by stellar oscillations or not. An example of these false frequencies induced in the spectrum due to the time of the measurements are so-called *alias frequencies* and the most famous example is the one-day alias present in ground-based data due to the rotation of the Earth. This is an important source of complications that is avoided with space photometry.

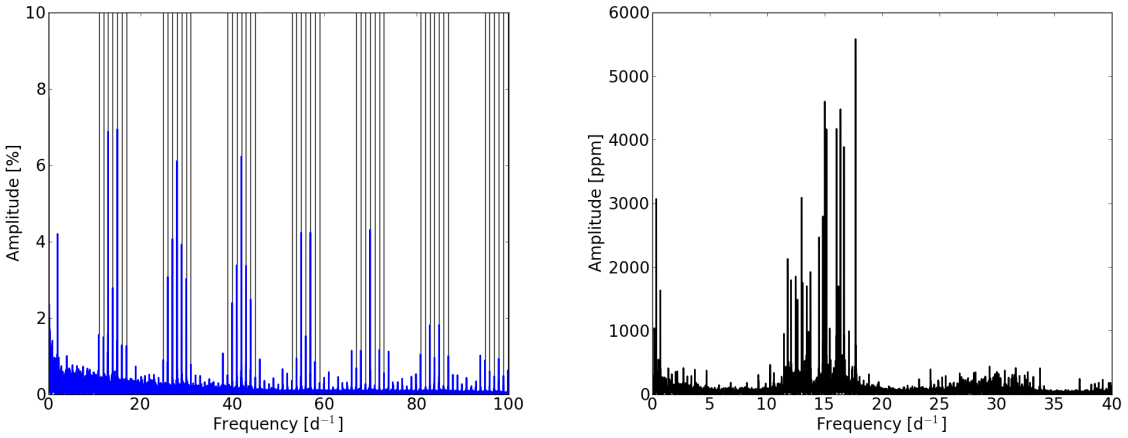

(a) (b)

Figure 2.3: Computed spectral window (blue) including the frequencies related to CoRoT (grey) (a) and complete Fourier spectrum (b) of the data set.

The plot of the spectral window (Figure 2.3(a)) was truncated to appreciate all the alias features as the amplitude of the highest peaks is less than 8%. Most of the frequency peaks that are present in it are related to the satellite and correspond to its orbital frequency of 13.972 d^{-1} and its aliases. All the frequencies related to CoRoT are known and given by the CoRoT team (Auvergne et al., 2009) so they are easy to exclude from the list of detected frequencies. In the plot of the spectral window they have been indicated with grey lines. There is one alias peak with remarkable amplitude ($\sim$ 4% of the amplitude) at $\sim$2 d^{-1} that was not marked as a CoRoT-related frequency. It probably rises due to the passes of CoRoT by the SAA that occurs twice a sidereal day and was the cause of most of the rejected points.

Before starting with the frequency extraction, the average noise level of the frequency spectrum was computed. This was done using different frequency intervals and, in general, the highest noise levels (200 - 300 ppm) were found at the frequency ranges below 1 d^{-1} and between 10 and 19 d^{-1}. This makes sense when the spectrum is observed as those are the ranges where the dominant frequencies are present and this analysis does not differentiate real peaks from noise. Outside the regions where the frequencies are, the average noise level of the data is always below 90 ppm.

The described iterative fitting and pre-whitening procedure was performed in order to account for all the present frequencies for which a chosen significance criterion was satisfied. A frequency was considered to be significant when its signal-to-noise ratio (S/R) was higher than 4.0 (Breger et al., 1993). This was ascertained for each detected frequency using the pre-whitened data and a box of one cycle per day to compute the noise level. The result depends on the choice of the frequency box size and for frequencies that are at

the end of the list, it can mean the difference between being considered statistically significant or not. Several box values were tested for the last frequencies but in our particular case, the first not-included frequency had S/R < 4.0 independently of the box size while the last frequency that was considered significant was also significant for all the different box sizes tested.

In Appendix A, the complete list of extracted frequencies is presented together with the amplitudes and phases obtained from the least-squares fitting performed with Period04. The numbers in brackets indicate the uncertainty associated to the last decimal digit presented. These were computed with the following formulae (Aerts et al., 2010),

$$\sigma_\nu = \frac{\sqrt{6}\sigma_N}{\pi\sqrt{N}AT}, \qquad \sigma_A = \sqrt{\frac{2}{N}}\sigma_N, \qquad \sigma_\delta = \frac{\sigma_N}{\pi\sqrt{2N}A}, \tag{2.2}$$

where N is the number of data points, σ_N is the average error on those and T is the total time covered by the data set. It is important to be aware of the fact that these formulae are only valid for the case of uncorrelated white Gaussian noise and must therefore be considered as too optimistic when working with real data.

In total, 90 frequencies have S/N > 4.0. After checking that alias frequencies related to the CoRoT orbital frequency were not present in the list, Figure 2.4 shows a noise-free

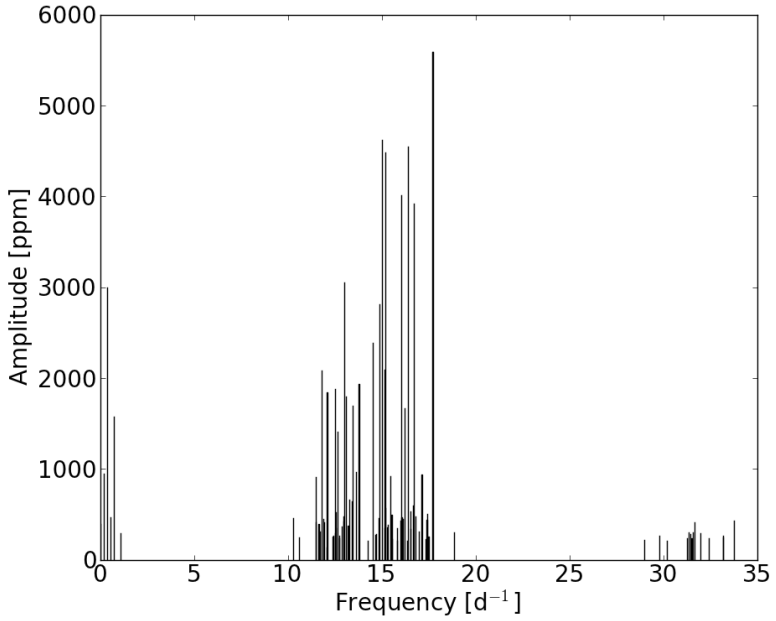

Figure 2.4: Power spectrum of the 90 detected oscillation frequencies of HD 41641.

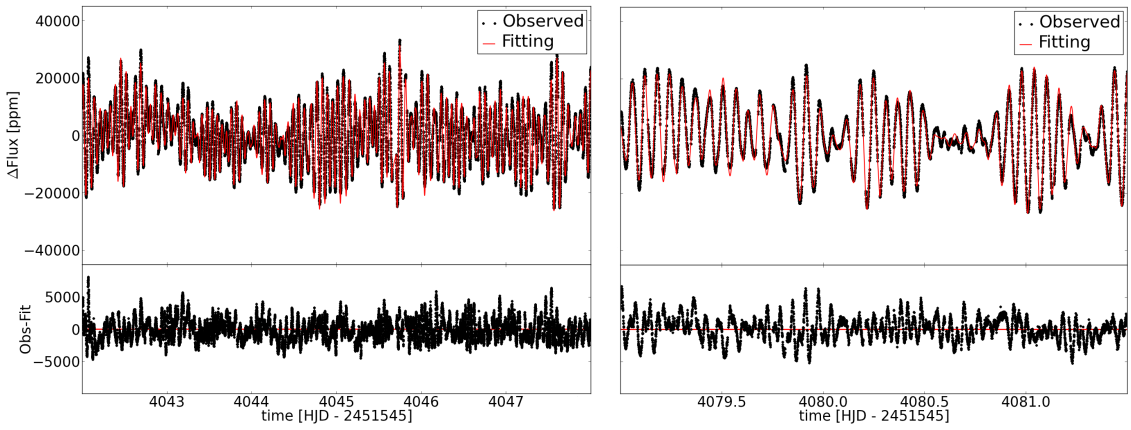

(a) (b)

Figure 2.5: Subsets of the observed light curve and the model generated from the 90 detected frequencies.

frequency spectrum that includes all of them. Figure 2.5 shows how the synthetic light curve generated with the sinusoidal contributions of the 90 frequencies fits the data using the same subsets as in Figure 2.2. The residuals can be observed in the lower panels and they still present some regular patterns. It is likely that with a less strict significance criterion more oscillation frequencies can be found but in the present study we restricted ourselves to frequencies for which S/N $>$ 4.0.

Figure 2.4 shows that the oscillation frequencies of the target are organized in three main groups of peaks. Two of them, those at higher frequencies, are inside the expected range for a δ Sct star and will be deeply analyzed in Section 2.3.3 but the peaks of the leftmost group cannot correspond to intrinsic p-mode oscillations of a pure δ Sct star. They will be closely studied in Section 2.3.3.

2.3.2 Frequency analysis: the low frequency range

In Figure 2.6, the low frequency peaks can be better observed. First of all, the leftmost peak, found as the 50th frequency with a value of 0.013955 $\pm$ 0.000008 d^{-1}, was considered to be too small to be pulsation-related. It does not appear in the list of known frequencies caused by CoRoT so it seems not to be caused by instrumental effects and it does not match the inverse of the length of the data set ($1/T \sim 0.01059$ d^{-1}) either. It might be related to other physical effects such as an orbital motion or rotation and we will recover the analysis of this possibility later. The other five low frequency peaks form a series of harmonics evenly spaced by the value of the lowest one. This frequency

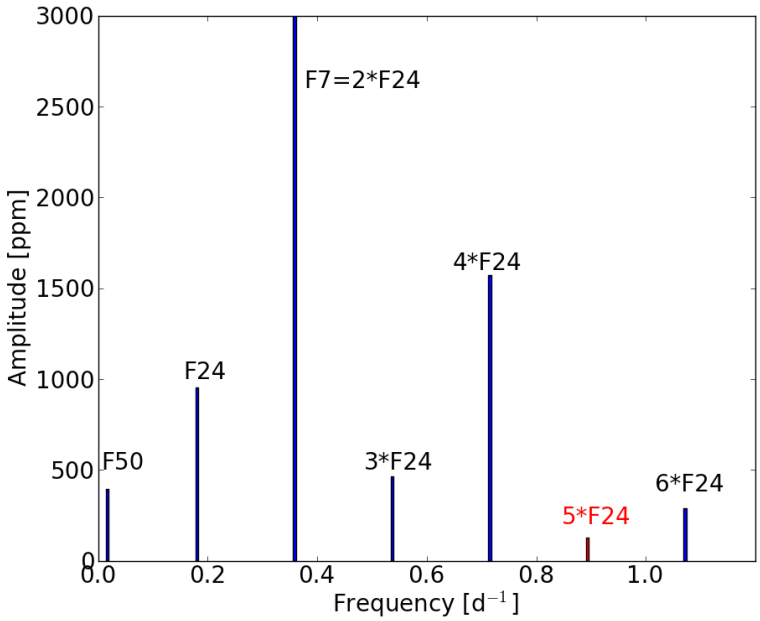

Figure 2.6: Low frequency range of the power spectrum of HD 41641. The fifth peak of the observed harmonic series is added in red as it was found not to fulfill the significance criteria (S/N $\sim$ 3.0).

was named F24 in the list. There are two important characteristics of the series that should be mentioned. One is that the peak which appears with the highest amplitude (7th in amplitude considering the complete list of found frequencies) is the second one (F7=2*F24) instead of F24 itself. The second one is that the fifth multiple of F24 is missing probably due to a low signal-to-noise ratio.

As a first step before trying to analyze these low frequencies, the missing fifth peak was searched. As the expected value is approximately known, in order to look for it in an efficient way, the described analysis was repeated but applied only to a range between 0 and 1 d^{-1}. A value of 0.8902 $\pm$ 0.0002 was found with S/R $\sim$ 3.0 and was included in red in Figure 2.6.

Low frequencies detected in δ Sct stars outside the p-mode range can have different explanations. The first one is that they can simply be caused because of combinations between peaks that are present at higher frequencies. This was checked (see Section 2.3.3) and relations were not found to explain the presence of all these peaks within the error bars which were established to perform the analysis. In addition, this situation could generate random low frequency peaks but it is not probable that they appear as a complete series of harmonics as it happens here. These frequencies could also be g-modes, typical γ Dor frequencies that would make the target to be a hybrid pulsator instead of

a pure δ Sct star. A lot of this type of oscillating stars have been reported since the era of space-photometry started (see Uytterhoeven et al. 2011) and they are very interesting targets but again, the clear harmonic structure does not support this possibility. There are two more plausible scenarios which are totally compatible with the observed structure. These are binarity and stellar spots on the surface of HD 41641.

In the case that the star had an orbital companion in the line of sight, its passes in front of the studied star would cause periodic reductions of the detected flux. This periodic eclipses would create depths in the light curve that could not be well-described with a single sinusoidal function. It would be also possible that this orbital companion is not in the line of sight but it is in a relatively close orbit and slightly distorts the shape of primary component leading to light variations as it moves around its orbit. Both scenarios would justify the presence of the harmonics and one of the peaks would correspond to the orbital period of the system. In addition, Poretti et al. (2005) suggested that HD 41641 could be a double-lined spectroscopic binary.

The other explanation that could justify these peaks is the presence of spots on the surface. These are regions on the photosphere that are brighter or darker than their surroundings. When a dark (bright) spot is in the part of the star that is visible by the telescope, a reduction (increase) in the detected flux is noticed. Then, the fundamental peak of the series would be related to the rotation period of the star. As in the case of the presence of a orbital companion, the features that would be generated in the light curve could not be properly described by a single sine curve and this would explain why multiples of the rotation frequency appear in the Fourier spectrum.

It is not trivial to distinguish between these two possible scenarios and it is not possible to do it using only photometric data. It is also difficult to unambiguously identify which peak is the one related to the physical mechanism, i.e. orbital motion or rotation. The first peak of the series would be the logical choice but the second one is the one that appears with the highest amplitude. Only with the available spectroscopic data it will be possible to investigate this feature (see Section 3.2).

A low-pass band filter was applied to the light curve in order to filter out the high frequencies and visually inspect the light curve generated by the low frequencies. The upper panel of Figure 2.7 shows a subset of the data set where the original measurements can be observed and the filtered light curve is overplotted. In the lower panel, the contribution of the low frequencies can be better observed and as expected and explained before, it is difficult to describe its features with a single sine (or cosine) curve, so higher order harmonics are necessary to reproduce this curve.

We applied another test to investigate the low frequencies by using the Phase Dispersion Minimization (PDM) method, first derived by Stellingwerf (1978). In contrast to the Fourier analysis described before which assumes that the data can be described by

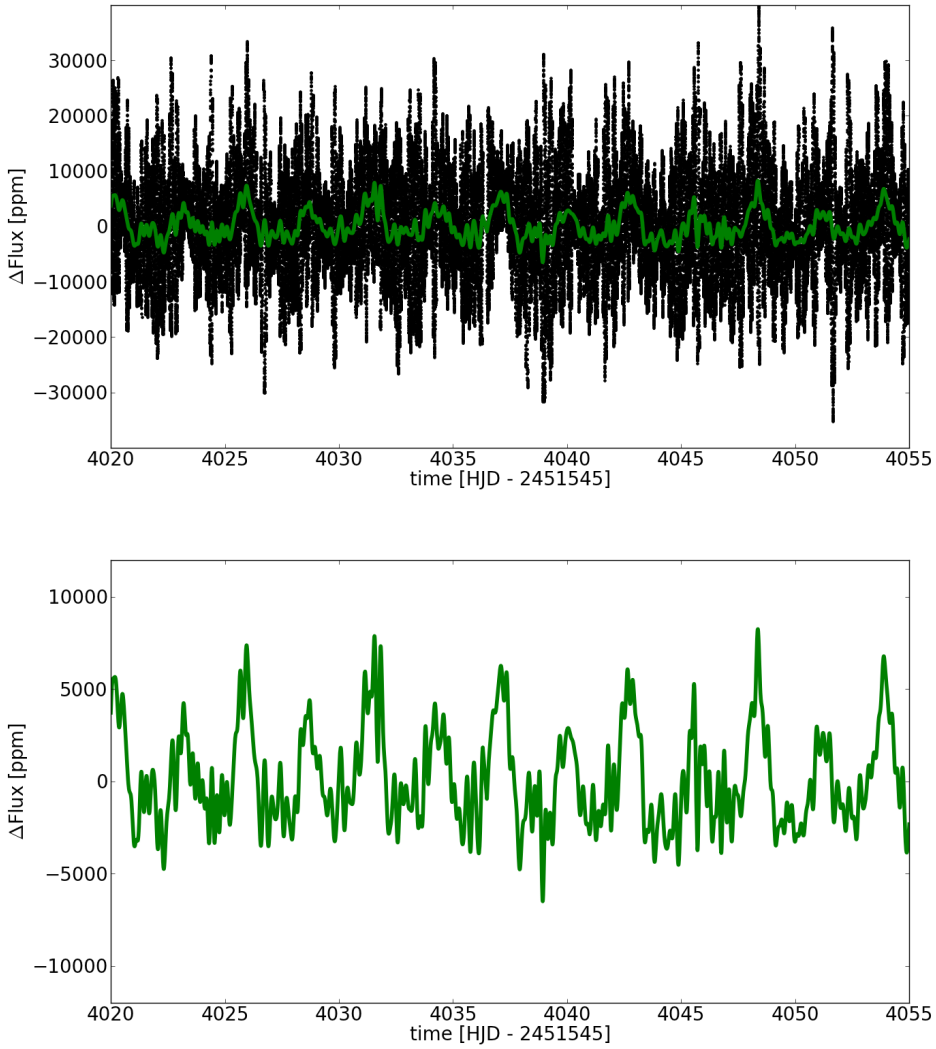

Figure 2.7: Subset of the light curve (black dots) and contribution of the low frequencies to it (green line).

the combination of a finite number of sinusoidal curves, the PDM is a non-parametric approach, i.e. it does not assume any model function to describe the data. During the procedure, the data is folded and plotted versus phase using different test frequencies. When the data is truly periodic with one of those frequencies, the folded data will create a clean curve while if that is not the case, the result will be pure scatter. The PDM method requires that the spread of the data around the average curve in the phase diagram reaches a minimum. If the ratio of the variance obtained for each test frequency over the total variance is plotted against the whole frequency range, this function will reach a local minimum around a true frequency. On the other hand, for a false frequency, the ratio will be approximately unity (Aerts et al., 2010).

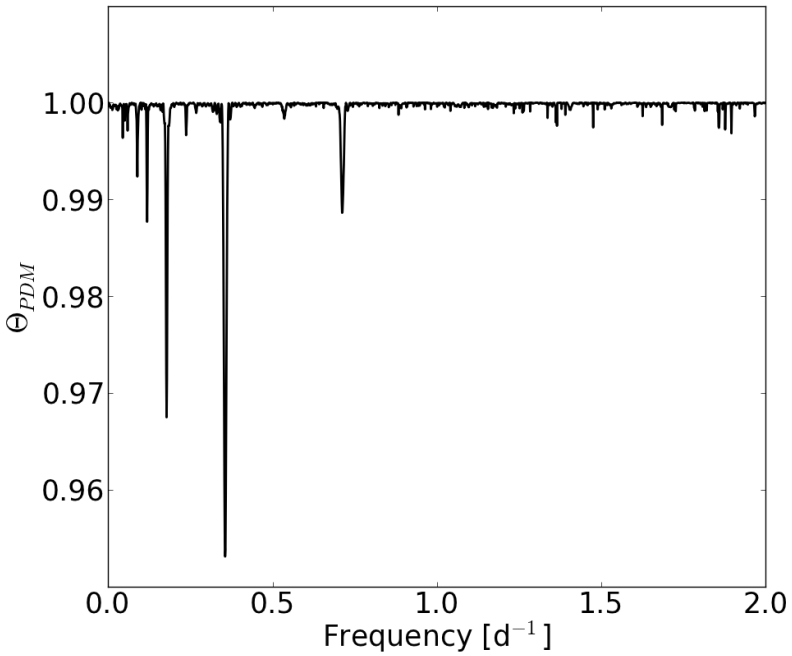

Figure 2.8: Phase Dispersion Minimization (PDM) method applied over the low frequency range of the photometric data set.

Figure 2.8 shows the obtained result when the PDM method is applied over the low frequency range. As it was the case when the Fourier technique was applied, the second multiple of the series of harmonics (F7 = 0.35603 ± 0.00001 d^{-1}) can be observed to dominate over the first one (F24 = 0.177556 ± 0.000003 d^{-1}) (see Figure 2.6). It will still be necessary to include the spectroscopic analysis to conclude which one of the described scenarios, binarity or spots on the surface, is the responsible of these low frequency peaks but F7 will likely be the physically meaningful frequency. This effect of the second peak being the dominant one implying that there are half multiple harmonics in the series has been observed before in δ Sct stars, e.g. Lampens et al. (2013) or Lehmann et al. (2006).

2.3.3 Frequency analysis: δ Sct p-modes

The other two groups of frequencies correspond to δ Sct-type p-mode frequencies (see Figure 2.9). Relations between peaks, regular spacings and other possible regularities were investigated in both the frequency and the period domains. Hence, the uncertainty associated to each frequency becomes important. A frequency peak will be considered not to be caused by an intrinsic oscillation but by the combination of two other frequencies when its value and the sum of the other two are equal within the errorbars. As it was

already mentioned, the error estimates presented in Equation (2.2) are lower limits for these errors. They were hence considered as lower limits for the uncertainties in the search for regularities.

There is also a theoretical limit for the frequency resolution known as the *Rayleigh criterion*. It associates a much bigger error to each frequency that equals the frequency resolution, $\sigma_R = 1/\mathrm{T}$, where T is the total length of the data set (see Table 2.1). This is just a rough estimate of the reachable accuracy because it does not take into account the signal-to-noise ratio of the amplitudes and the noise level of the data. Within 1/T, two different frequencies could be considered to be the same and many spurious frequency relations could be detected. For this data set, $\sigma_R = 0.01059$ d^{-1} while the average error computed with the Equations (2.2) is about 0.00005 d^{-1}. There is a wide range of possibilities between these two limits that was carefully inspected in the course of our analysis.

First, combinations of frequency peaks were searched. As it was said, a frequency, F_i, was considered to appear due to the combination of two (or more) others when the difference between that frequency and the result of the sum of the others ($F_j + F_k$) was smaller than the combination of the errors σ_F computed by error propagation as indicated in Equation (2.3):

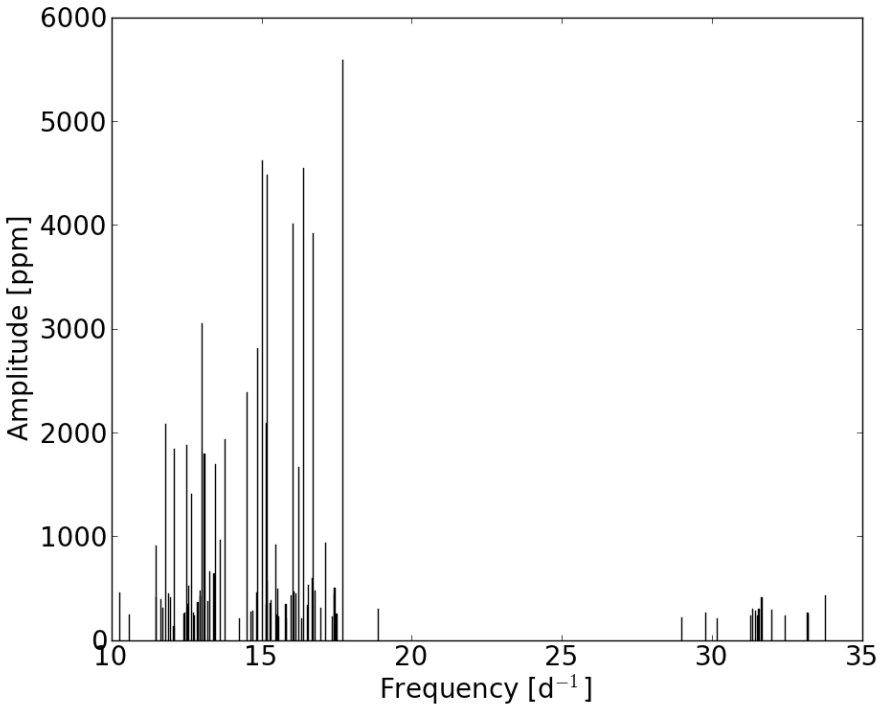

Figure 2.9: δ Sct p-mode frequencies of HD 41641.

$$F_i = F_j + F_k \iff \mid F_i - (F_j + F_k) \mid < \sqrt{(a\sigma_{F_i})^2 + (a\sigma_{F_j})^2 + (a\sigma_{F_k})^2}, \qquad (2.3)$$

where a is a factor that will be used to increase the theoretical uncertainties given in Equation (2.2). As a first approach, it was chosen to be 1 and, after that, results given by a=2, 3, 5 and 10 were also analyzed.

The last column of Table A.1 in Appendix A includes all the identified relations where the superscript indicates the value of a that was used when it was detected. No alias peak caused by any of the CoRoT-related frequencies was found within the 10σ uncertainty level. Note that all the relations that included F50 = 0.013955 $\pm$ 0.000008 d^{-1} were ignored because this value is close to the frequency resolution and in a Fourier spectrum with such a high peak density, it could generate a lot of spurious frequency relations.

Using the 10σ uncertainty (i.e. an average error of 0.0001 d^{-1}), every peak present in the rightmost group could be explained as combination of two frequencies of the intermediate frequency group and one of the low frequency peaks. This is important to exclude this range of frequencies as independent frequencies of the target and is in full agreement with the recent study by (Kurtz et al., 2015). Hence, the oscillation frequency range of HD 41641 is reduced to the range between 10 and 20 d^{-1}. The 10σ uncertainty is also enough to relate the low frequency peaks with each other confirming what was seen by eye, they form a series of harmonics.

Relations were also found between peaks of the p-mode range, all of them concerning one of the low frequency peaks. It may be possible that those relations are justified by rotational splitting but the high density of peaks in the Fourier spectrum makes its analysis quite complicated. Also no clear multiplet was found in spite of the amount of found relations. It is possible that they could be found if higher values of a were used but, as it was mention before, there are peaks which are very close to each other and it is unclear if they form frequency series.

Finally, the Fourier spectrum was also studied in the temporal domain and is included in Figure 2.10. The period peak at 1/F50 = 71.659 days was not plotted for clarity. The structure of the low frequency peaks can be observed again at periods of a few days and a really dense region is found between 1 and 2.5 hours corresponding to the p-mode frequencies. No new regularities were found but as it was said before, the amount of peaks hinders more solid conclusions.

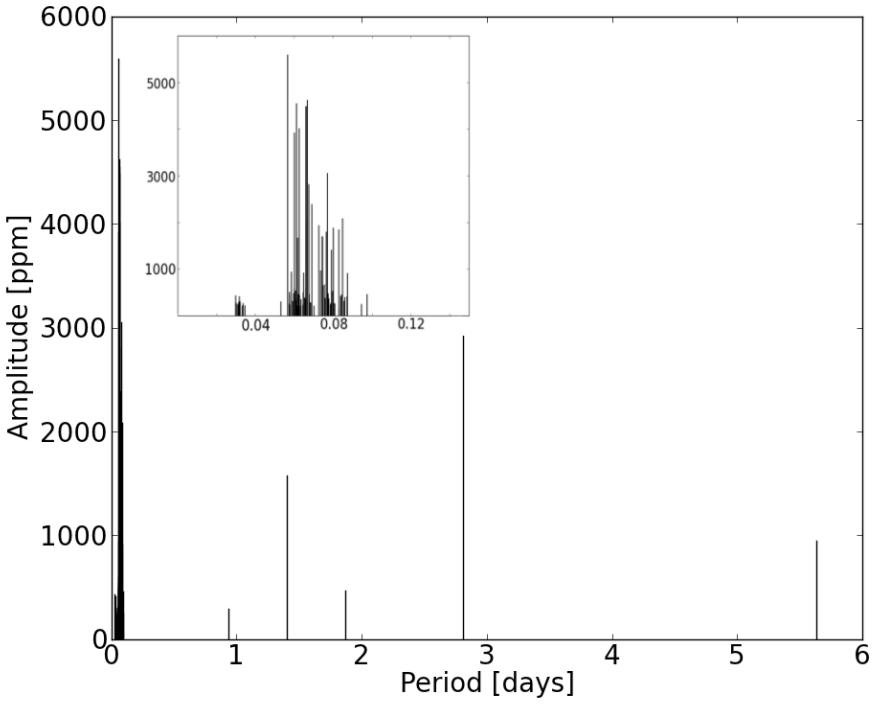

Figure 2.10: Period peaks found in the Fourier spectrum of HD 41641.

2.3.4 Frequency analysis: Amplitude variability

From the study of the complete light curve, 90 frequencies and their corresponding amplitudes were detected. It is possible that these detected amplitudes change over time. In order to test this, the temporal amplitude variability was studied. Amplitude variability has previously been observed and studied for δ Sct stars, e.g. Bowman & Kurtz (2014).

The light curve was divided in 10 subsets of 10-day length with an overlap of one day with the previous and the next subsets. Table 2.2 summarizes the start and end times of each light curve and lists the detected frequencies with S/N $>$ 4.0 ordered by decreasing amplitude. Naturally, less frequencies were detected in comparison to the analysis of the complete data set. This is an excellent illustration of how important the acquisition of long and continuous observations is to carry out asteroseismic studies. Only the eight highest frequencies of the complete set appear as significant frequencies in the 10 sections (but F4 that was not found between the significant frequencies in the last subset), hence only those were studied.

In Figure 2.11 the ten measured amplitudes of the eight studied frequencies are plotted against the central time of the 10-day subset light curves and connected with a continuous line. A different color is used for each frequency and the dashed straight line of the

Table 2.2: Time limits and frequencies detected for each light curve subset.

Light curve	**Fist time point [HJD-2451545]**	**Last time point [HJD-2451545]**	**Detected frequencies**
LC1	4003.356	4013.356	F1,F5,F2,F3,F9,F8,F7,F4,F6,F12, F10,F13,F17,F14,F15,F19,F18,F21
LC2	4012.356	4022.356	F1,F2,F3,F5,F6,F7,F9,F8,F10,F12,F4
LC3	4021.356	4031.356	F1,F3,F5,F6,F2,F4,F8,F7,F10
LC4	4030.356	4040.355	F4,F1,F3,F2,F8,F5,F6,F7,F12,F10,F9
LC5	4039.356	4049.354	F4,F1,F3,F2,F6,F5,F8,F7,F14,F9,F10,F12,F13 F15,F16,F18,F19,F20,F17,F25,F24,F22,F23
LC6	4048.352	4058.356	F4,F1,F2,F3,F6,F5,F8,F7,F10,F9,F13,F12,F17
LC7	4057.356	4067.356	F4,F1,F3,F5,F8,F2,F6,F7,F9,F10
LC8	4066.355	4076.356	F4,F1,F2,F3,F5,F8,F6,F9,F7,F10,F13,F12
LC9	4075.356	4085.355	F1,F5,F6,F3,F2,F4,F8,F7
LC10	4084.356	4094.355	F1,F2,F3,F5,F6,F8,F7,F9,F13

same color corresponds to the amplitude measured before for the complete light curve. The included error bars correspond to four times the theoretical uncertainties which were computed with equation (2.2) and included in Table A.1.

It can be observed that most of the frequencies slightly vary close to the dashed line. Some of those present a very small variability, e.g. F1, but there is a remarkable case that presents really strong variation over time: F4. There must be a physical reason why at certain times, but not always this oscillation mode is more prominent in amplitude. It is worth mentioning that F4 was not even detected in the tenth section having a S/N over the significance criteria and was searched afterwards and found with S/N $\sim$ 3.0.

Figure 2.12 represents the same plots observed in Figure 2.11 but in a separate panel for each frequency and including also the phase variability. The later was studied in the same way than the amplitude variability for the 10 same subsets. No apparent correlation is found between the amplitude and the phase variations, or at least not a common correlation for all the studied frequencies.

In order to study the strong variability of F4, Figure 2.13 shows the Fourier spectra of the ten subsets around this peak. The variation is clear, especially if these plots are compared with those in Figure 2.14 where the same was done for F1, the frequency with the most stable amplitude. If the variability is considered to be periodic, its period can be estimated from Figure 2.11 and it can be measured to be about 72 days. This value is the inverse of F50, the lowest detected frequency which was not successfully explained

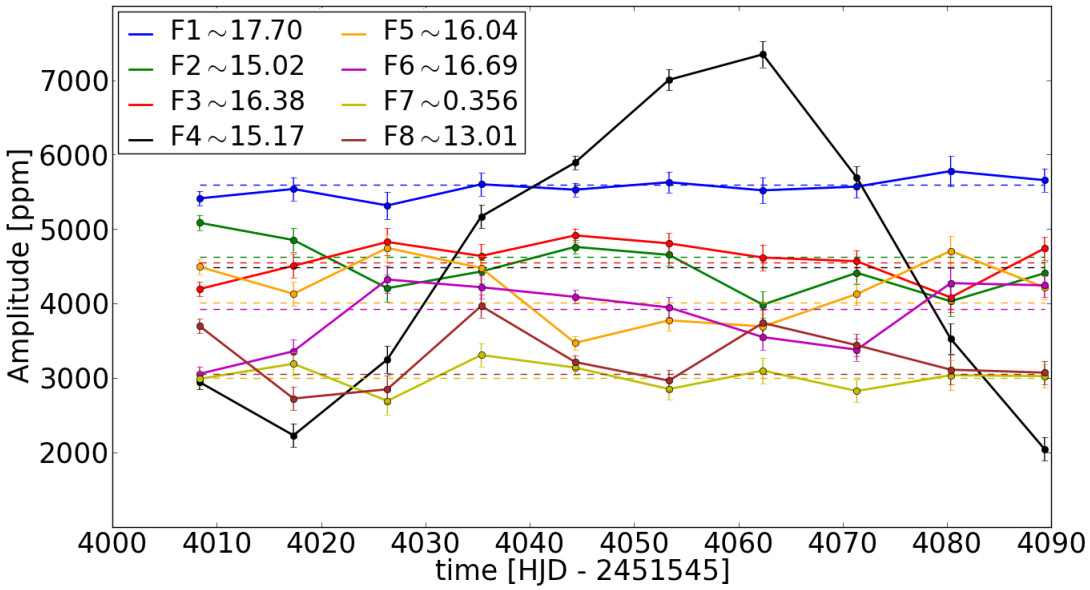

Figure 2.11: Study of the amplitude variability of the eight highest peaks.

in Section 2.3.2. Hence, the only frequency peak with completely unknown origin can be now justified to appear due to the periodic variation of the amplitude of F4. It would be interesting to have a longer data set to be able to cover more than one period and study this strong variation.

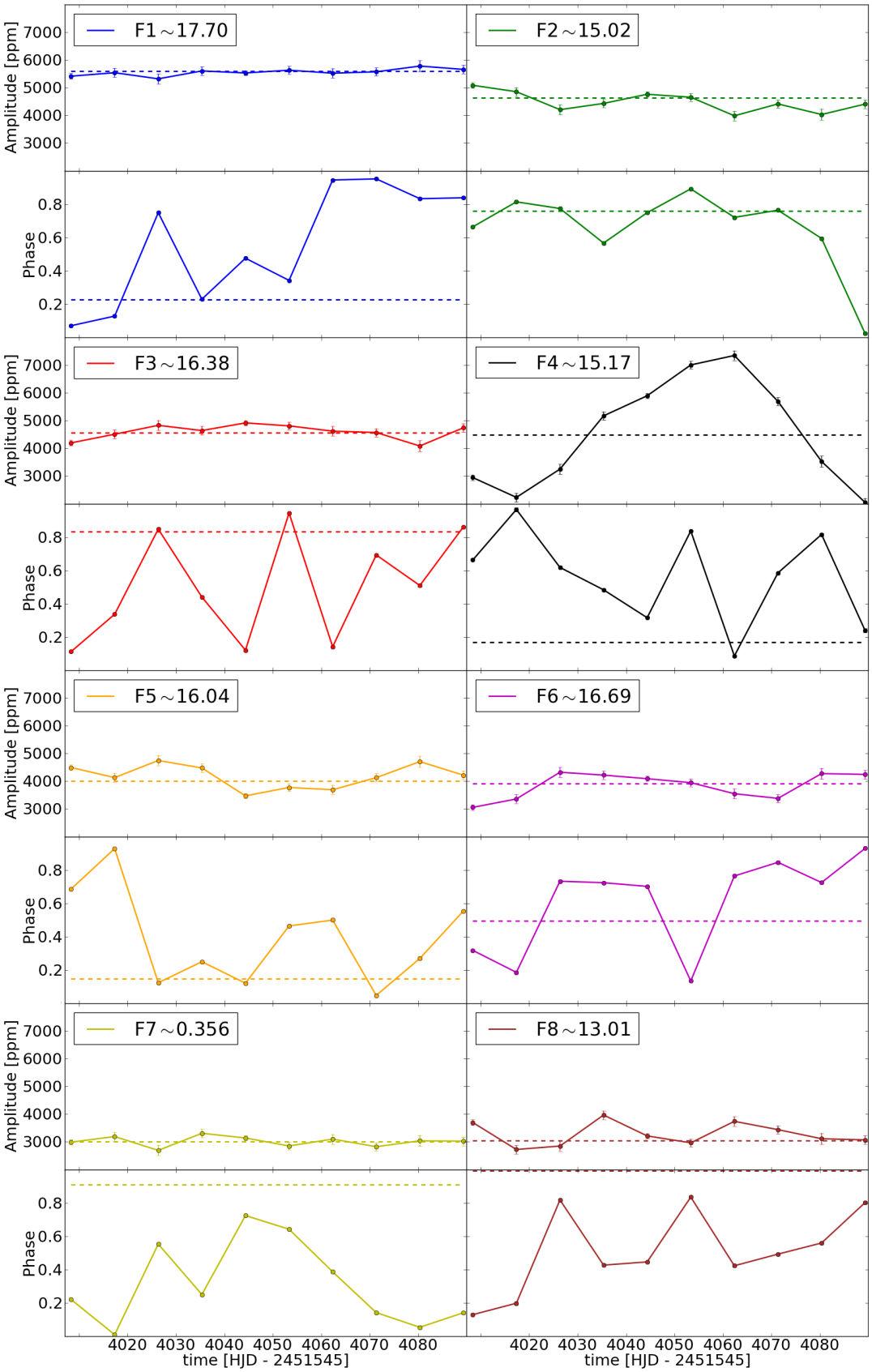

Figure 2.12: Amplitude and phase variability of the eight highest peaks.

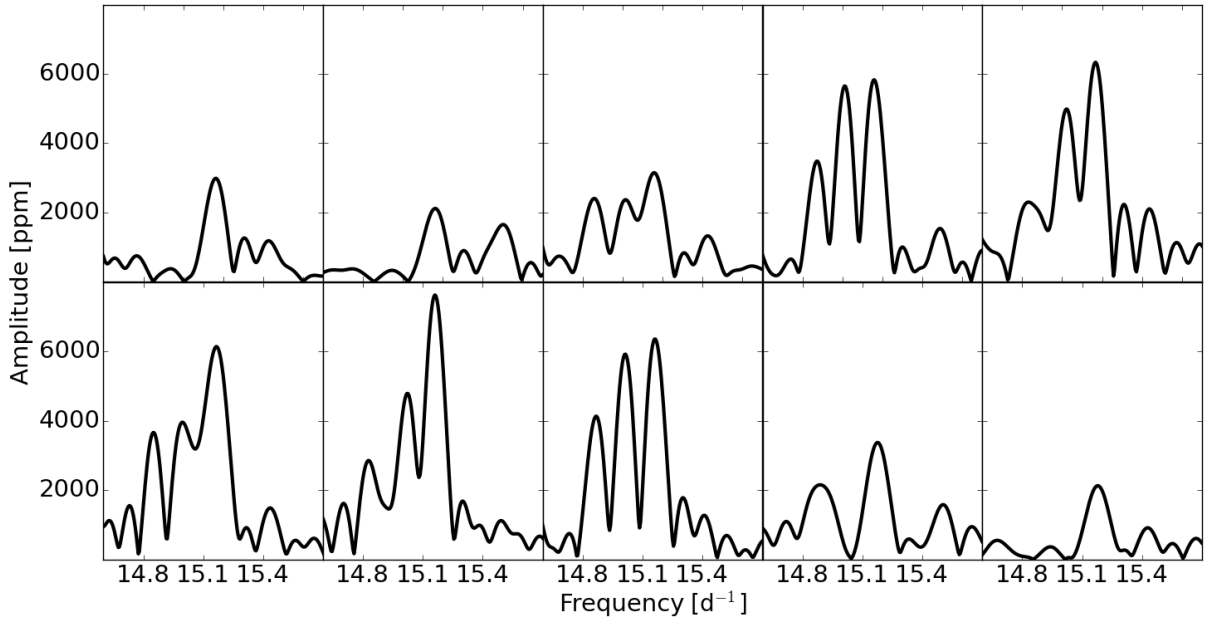

Figure 2.13: Series of Fourier spectra based on 10-day subsets to show the amplitude variability of F4.

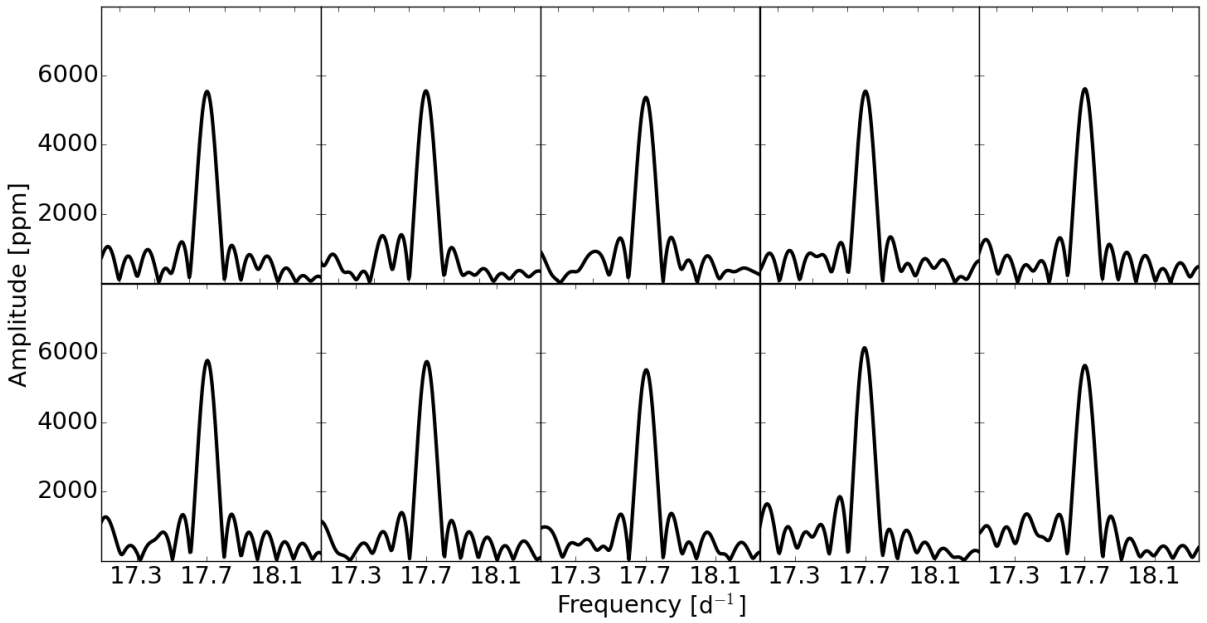

Figure 2.14: Series of Fourier spectra based on 10-day subsets to show the amplitude stability of F1.

Chapter 3

HARPS high-resolution spectroscopy

3.1 Spectroscopy for CoRoT targets with HARPS

To complement the photometric observations performed with CoRoT, ground-based spectroscopic campaigns where scheduled with the aim of having photometric and spectroscopic time series simultaneously obtained. These observations involved several high-resolution échelle spectrographs throughout the world (Poretti et al., 2013): FEROS and HARPS at the European Southern Observatory (ESO) in La Silla (Chile), FORCES at Calar Alto (Spain), SOPHIE at the Observatoire Haute Provence (France) and FIES at NOT and HERMES at Mercator, both at the Observatorio Roque de los Muchachos (Spain).

The first ESO Large Program with the goal of complementing the CoRoT mission was performed with FEROS and consisted of a total of 60 observing nights beginning in February, 2007 and coinciding with the CoRoT initial run (IR01). The FEROS instrument is a high-resolution échelle spectrograph which is installed on the 2.2 meter telescope operated at ESO-La Silla in Chile. Its high efficiency, large wavelength range covered and high resolution (R = 48000) make possible a large variety of stellar and extra-galactic spectroscopic observation programs requiring high spectral stability (Kaufer & Pasquini, 1998).

After the completion of this first program, Poretti et al. obtained two Large Programs (from December, 2008 to December, 2009 and from June, 2010 to January, 2013) with the HARPS spectrograph to obtain high-resolution spectra for selected CoRoT asteroseismic targets. HARPS stands for High Accuracy Radial velocity Planet Searcher and, as its name indicates, this high-resolution (R = 110 000) échelle spectrograph is a famous planet hunter that was built to measure radial velocities to a very high precision. The highly controlled environment where it is located, the achieved mechanical stability and the use of a Thorium-Argon lamp for instantaneous wavelength calibration allow that the

instrumental drifts during the night never exceed 1 m/s or even lower values in favorable situations (Lovis et al., 2006). The instrument was installed in 2002 on the 3.6 meter telescope at ESO-La Silla, in Chile, and since its first operation, more than 130 planets have been discovered with it. Some of those planets are habitable super-Earths of a strong scientific interest. Exoplanet hunting is not the only branch of astronomy that can take benefits of such an instrument. High-resolution spectra make the detection of high-degree oscillation modes possible. The high obtainable signal-to-noise ratio helps to detect small variations in the line profiles and allows to identify what kind of modes are being excited. For this reason, some of the CoRoT asteroseismic targets were included into the HARPS Programs and HD 41641 was among them.

3.2 Observations and data reduction

HD 41641 was observed during the second HARPS Program, during 15 nights between December 23, 2010 and January 12, 2011 overlapping with part of the photometric observations. The data set that was used for this project consists of 222 high-resolution spectra. Table 3.1 summarizes the information of the spectroscopic observations grouped by observing night.

The flux measurements covered the whole spectral range of HARPS, from 3780 to 6914 Å, and were distributed within its 72 spectral orders. They had been reduced using a semi-automated reduction pipeline developed by the HARPS Consortium. During this process, a sequence of extraction and calibration methods is applied to each raw spectrum. The 222 data files contained the barycentric corrected wavelengths, the unnormalized flux and the automatically normalized flux together with concrete information about each observation such as the heliocentric Julian Date at mid-exposure, the exposure time, or the mean signal-to-noise ratio (see summary per night in Table 3.1).

The normalization of the spectra is an important first step of the spectroscopic analysis and it is crucial for obtaining reliable results in asteroseismology. Hence, the pipeline normalized flux was not used and a careful normalization was conducted following the procedure developed in Pápics et al. (2012). The spectroscopic analysis was divided in three tasks whose normalization requirements were quite different from one to the other. These three main tasks were (i) the determination of the fundamental stellar parameters, (ii) the discernment between the two mentioned physical scenarios that might be causing the observed peaks in the low frequency range, and (iii) the study of the spectral line variability with the goal of identifying the oscillation modes. For the determination of the stellar parameters, a wide wavelength range was necessary and the 222 spectra were normalized in a range between 4500 Å and 5800 Å. On the other hand, to study the line variability, individual absorption lines had to be analyzed so the selected lines were individually normalized for the 222 spectra. In this case, a much smaller wavelength range

Table 3.1: Summary of the information of the spectroscopic observations grouped by observing night with HARPS. Note that the S/N of each spectrum was computed in the line free region [5805 Å - 5825 Å].

Date	Number of spectra	HJD begin	HJD end	S/N range	Exp.time range [s]
December 23, 2010	16	2455553.54	2455553.87	[170.1, 215.8]	[1100, 1200]
December 24, 2010	15	2455554.54	2455554.85	[125.4, 225.2]	[1100, 1200]
December 25, 2010	16	2455555.53	2455555.85	[136.2, 237.95]	[1000, 1200]
December 26, 2010	17	2455556.53	2455556.85	[147.35, 213.35]	[1050, 1200]
December 27, 2010	16	2455557.53	2455557.84	[142.7, 221.65]	[1050, 1200]
December 28, 2010	16	2455558.53	2455558.83	[151.1, 237.8]	[1000, 1200]
December 29, 2010	15	2455559.53	2455559.83	[125.1, 226.2]	[1200, 1200]
December 30, 2010	15	2455560.54	2455560.83	[170.3, 215.35]	[1000, 1200]
December 31, 2010	15	2455561.55	2455561.83	[171.0, 209.7]	[1100, 1200]
January 1, 2011	15	2455562.54	2455562.83	[164.25, 219.35]	[1000, 1200]
January 8, 2011	12	2455569.53	2455569.81	[139.75, 193.5]	[1200, 1200]
January 9, 2011	12	2455570.57	2455570.81	[164.9, 203.4]	[1100, 1200]
January 10, 2011	14	2455571.53	2455571.80	[132.6, 224.75]	[1100, 1200]
January 11, 2011	14	2455572.52	2455572.79	[161.3, 211.35]	[1050, 1200]
January 12, 2011	14	2455573.52	2455573.80	[179.6, 217.4]	[1050, 1200]

of 2-4 Å was used. For each line, this range was centered on its rest wavelength, λ_0. More information about the line selection and the λ_0 of each line is included in Table 3.5 and in Section 3.5.1.

The normalization procedure in both cases is similar: a function is fitted to the continuum, which was defined by some tens of points at fixed wavelengths. These points are manually chosen where the continuum is known to be free of spectral lines or telluric features. For the case of the widest wavelength range, the fitting-continuum function was chosen to be a cubic spline while for the individual spectral lines, a linear spline function was used. For both cases the points used to define these functions were chosen in a two-step process. They were first defined over the non-normalized spectrum but were checked and corrected in a second step after the first rough normalization. This was performed using a semi-automatic script that also takes care of the order merging taking into account the signal-to-noise values in the overlapping ranges and correcting for the sometimes slightly different flux levels of the overlapping orders. The script also returns the average spectrum.

Figure 3.1 shows two selected interesting regions of the normalized spectra: one of the

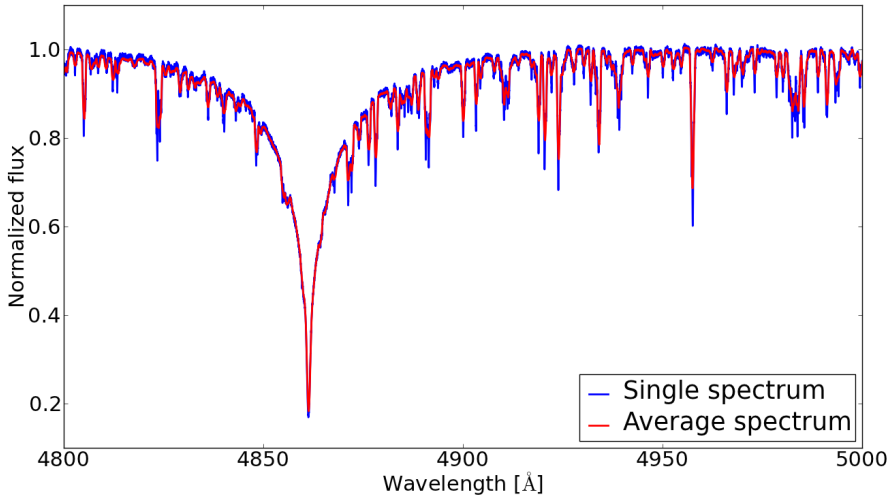

(a)

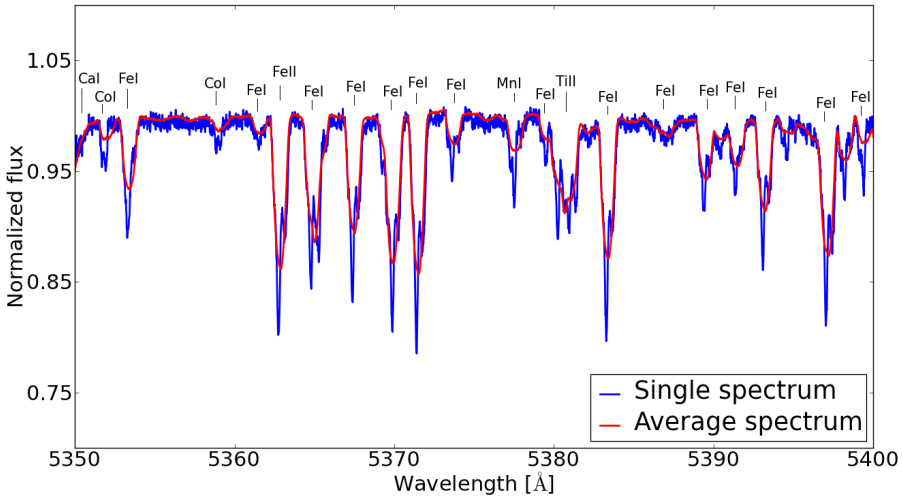

(b)

Figure 3.1: Hβ line (a) and a group of metal lines (b) for the first spectrum of the data set (blue) and the average spectrum (red).

Balmer Hydrogen lines, Hβ (a), and a group of metal lines (b). In this second section the elements associated to each absorption line were labeled. In both plots, the blue line corresponds to the first one of the 222 normalized spectra while the red line is the average spectrum.

3.3 Fundamental parameters and HR diagram

First the fundamental parameters of HD 41641 were determined. These included: the effective temperature ($T_{\rm eff}$), the surface gravity ($logg$), the metallicity ($[M/H]$), the projected rotational velocity ($vsini$) and the microturbulent velocity (ξ). With these characteristics, other important parameters, such as the stellar mass and radius can be also estimated.

The average normalized spectrum was analyzed with the GSSP (Grid Search in Stellar Parameters) code (Tkachenko et al., 2012) in order to estimate $T_{\rm eff}$, $logg$, $[M/H]$, $vsini$ and ξ. The code compares the observed spectrum with a series of synthetic spectra computed in a grid of the five considered parameters. It looks for the combination of these that minimizes the difference between the synthetic and the observed spectra in a χ^2 minimization procedure. The code makes use of the LLmodels code (Shulyak et al., 2004) to compute the atmosphere models and of the SynthV code (Tsymbal, 1996) to compute the synthetic spectra based on individual elemental abundances. All these codes are based on the assumption of local thermodynamical equilibrium (LTE), where the fraction FeII/FeI is described by ionization equilibrium (Saha equation) and the level populations are given by the Boltzmann equation.

As a first approach, wide ranges and big step sizes were used in order to cover the whole range of possible parameters. They were then progressively reduced in an iterative procedure. The wavelength range analyzed was from 4700 Å to 5700 Å, including the $H\beta$ Hydrogen Balmer line ($\lambda = 4861.3$ Å) and a wide region of metal lines. After using the average spectrum, the calculation was repeated using a single spectrum with high signal-to-noise ratio. The values obtained for the stellar parameters were the same within the error bars.

Table 3.2 summarizes the obtained results for HD 41641. The included uncertainties are those computed from the χ^2 minimization using a 1σ confidence level. Figure 3.2 shows the fit of the three spectra in the regions that were presented before. The grey line corresponds to the individual spectrum, the black line to the average one and the red one to the synthetic spectrum generated with the final stellar parameters. The residuals are the difference between the average and the synthetic spectra.

In Figure 3.3 the χ^2 values for the five variable parameters are presented. These values are high because the calculation was done using the average spectrum. The formula to calculate χ^2 includes the deviation of each data point in the denominator and for the average spectrum, this value is small and makes χ^2 increase. For the individual spectra, much smaller χ^2 values were obtained. In any case, it can be seen from Figure 3.3 that the five parameters are well constrained.

HD 41641 was included in a study of several CoRoT candidate targets done by Poretti et al. (2005). The values of $vsini$ (= 29 ± a few km/s) and $[M/H]$ (= -0.2 ± 0.2) presented in the mentioned paper are in perfect agreement with ours but their $T_{\rm eff}$ (= 7700 ± 200 K) and $logg$ (= 3.9 ± 0.2 dex) differ from our results. The methods used to determine the parameters are different: Poretti et al. (2005) used Strömgren $uvby\beta$ photometry while we determined our values from the much better suited high-precision spectroscopy.

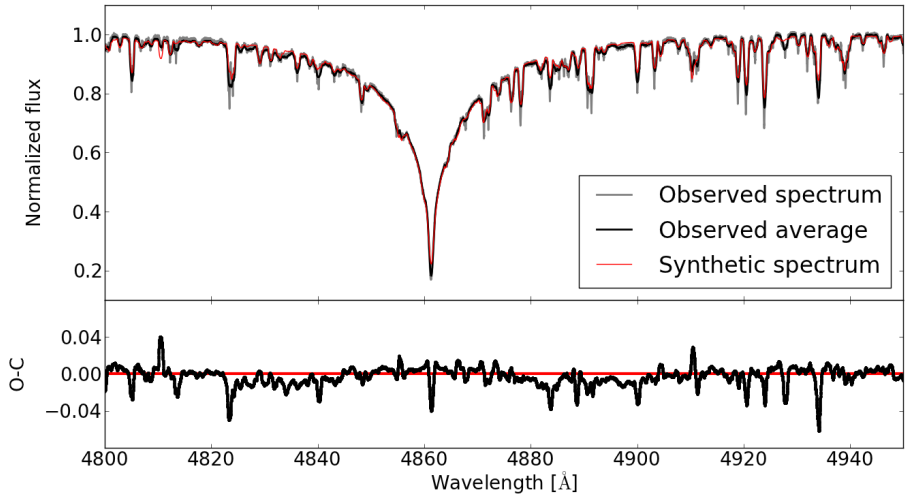

(a)

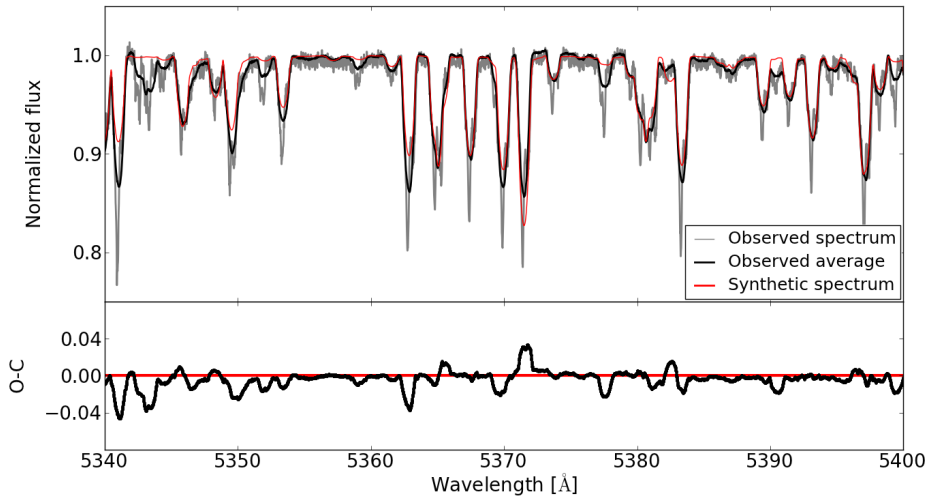

(b)

Figure 3.2: Fit of the synthetic spectrum (red) to the Hβ line (a) and a group of metal lines (b) for a single spectrum (grey) and the average spectrum (black).

Table 3.2: Stellar parameters obtained with GSSP for HD 41641

$T_{\rm eff}$	7200 ± 80 K
$logg$	3.5 ± 0.3 dex
$v\sin i$	30 ± 2 km/s
[M/H]	-0.19 ± 0.08 dex
ξ	1.1 ± 0.3 km/s

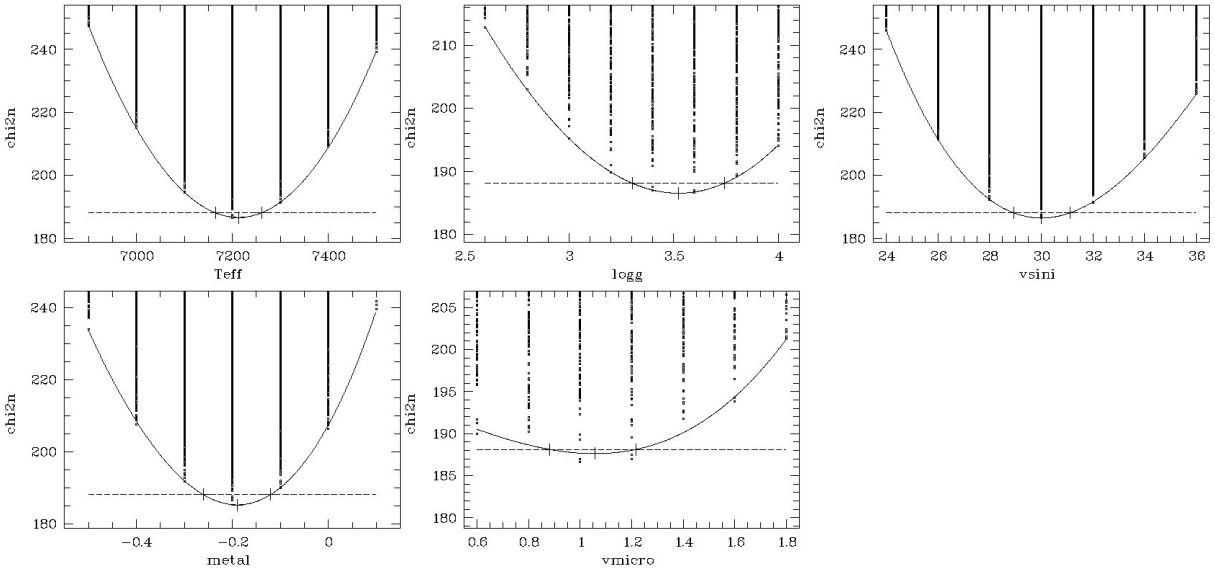

Figure 3.3: Results of the χ^2 minimization for the five studied parameters.

In order to actually compare both results, a synthetic spectrum was generated with GSSP using the four parameters from Poretti et al. (2005) and setting ξ as a free parameter in order to find the best fit obtainable with their values. The synthetic spectrum with $\xi = 1.9 \pm 0.3$ km/s gave the minimum χ^2 and can be seen in Figure 3.4 plotted in green together with our synthetic spectrum in red and the average observed one in black. There is not a big difference in the metal line region but from the fit of the Hydrogen line, it can be concluded that the parameters derived in this work give a better result.

The estimated values of $T_{\rm eff}$ and $logg$ allow to place the target into the HR diagram and constrain its mass. This is done in Figure 3.5 where the solid circle represents HD 41641 and the shaded box corresponds to the error bars obtained from the χ^2 minimization. The evolutionary tracks were taken from Guenther & Brown (2004). To generate these tracks Guenther & Brown (2004) constructed a dense grid of stellar models from known observational constraints of the oscillators, calculated p-mode frequencies for them and

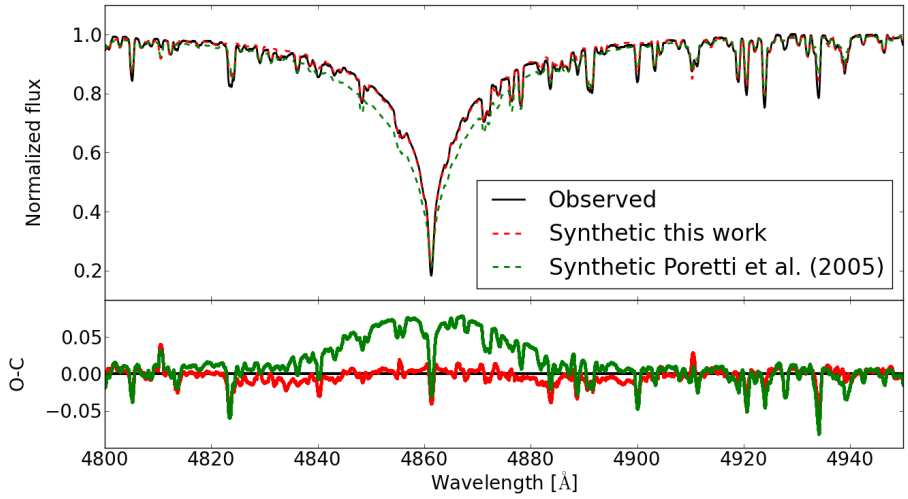

(a)

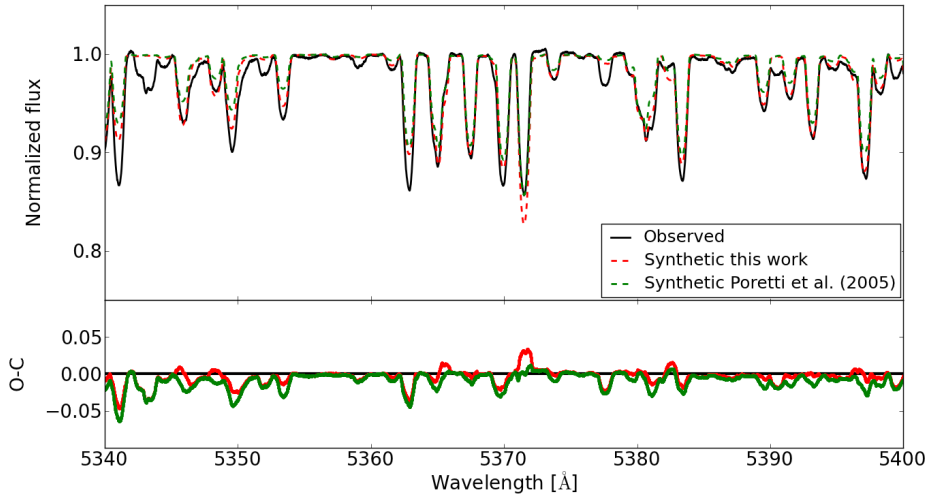

(b)

Figure 3.4: Comparison of our results with those obtained in Poretti et al. (2005).

compared with observed spectra to find the best fits. All stellar models were calculated using the Yale stellar evolution code, YREC (Guenther et al., 1992), and the OPAL98 opacity tables (Iglesias & Rogers, 1996). They have approximately 2000 shells. One-third of them cover the stellar interior, one-third cover the outer envelope and one-third cover the atmosphere which is treated as a gray atmosphere in the Eddington approximation. Convective overshoot and rotation are not included in the models and the mixing-length parameter used is $\alpha = 1.8$.

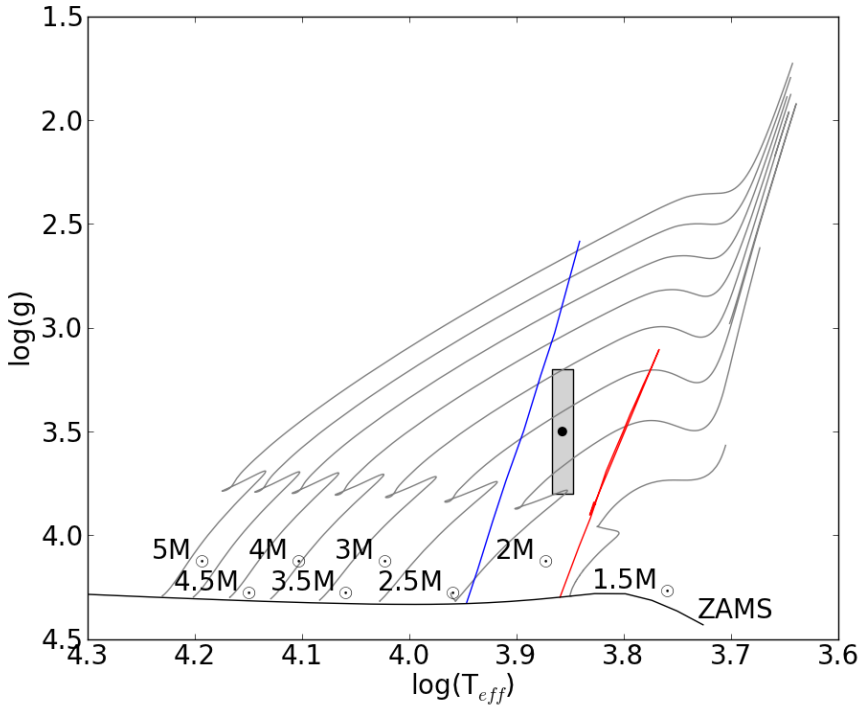

Figure 3.5: HR diagram including HD 41641. Zero Age Main Sequence, theoretical blue edge and empirical red edge of the classical δ Sct instability strip from Pamyatnykh, A. (private communication) and post Main Sequence evolutionary tracks from Guenther & Brown (2004).

The theoretical blue edge of the classical δ Sct instability strip and the empirical red edge are also plotted as well as the Zero Age Main Sequence (ZAMS) (Pamyatnykh, A., private communication). From this, we estimate the mass of HD 41641 to be M = 2.3 $\pm$ 0.7 M$_\odot$.

Finally, also the radius of the star can be estimated from the the derived *logg* and the estimated mass as indicated by equation (3.1),

$$g = \frac{GM_*}{R_*^2} \quad \Longrightarrow \quad R_* = \sqrt{\frac{GM_*}{10^{logg}}}, \tag{3.1}$$

where G is the gravitational constant, M_* and R_* are the mass and the radius of the star and g the surface gravity in cgs units. Taking into account the uncertainties of *logg* and M$_*$, the radius of the target can be estimated to be R_* = 4.5 $\pm$ 1.7 R$_\odot$. From the data of the evolutionary stellar models done by Guenther & Brown (2004), the radius of the target can also be estimated taking into account its position in the HR diagram and the values obtained are also within the computed range.

3.4 Origin of the low frequencies

3.4.1 Possible binary companion

From the CoRoT photometry, we discovered a harmonic series of peaks at low frequencies (see Section 2.3.2.) and suggested that they originate either from a binary companion or from spots on the surface of HD 41641. In Poretti et al. (2005), it is suggested that HD 41641 could be a double-lined spectroscopic binary. We therefore used the HARPS spectroscopic data set to test this hypothesis.

The combination of rotational and pulsational broadening lead to a low *vsini* (see Table 3.3) so the spectral lines are quite narrow. No periodical line shifting was detected upon visual inspection and comparison of the spectra. In order not to reduce our arguments to visual inspection a Least-Squares Deconvolution (LSD) analysis was conducted. In an LSD analysis an average line profile is created that represents each spectrum assuming that all its lines are similar in shape and can be represented by the same profile scaled in depth by a certain factor. It is also assumed that the intensities of overlapping spectral lines add up linearly. This technique increases the S/N enormously and makes it easier to study the line profile variations. More details about the extraction of the LSD profiles can be found in Tkachenko et al. (2013).

The HJD of each spectrum was converted into phase by using the dominant of the low frequencies (F7 = 0.35603 d^{-1}). To create Figure 3.6, the average of the 222 LSD profiles was subtracted from each individual profile and the relative fluxes are plotted covering the phase in a color diagram. Any feature of the LSD profiles of less flux than the average is colored in green while those of higher flux are colored in yellow. Two types of variations are observed in the relative flux. There is a yellowish band that seems to follow the phase and is probably related to the peaks in the low frequency domain and there are faster changes in the flux which are not coherent with the phase and are probably related to the p-mode frequencies. However, the most important fact that can be concluded from this plot is that there is not radial velocity shift of the profiles following the phase as it would be expected if HD 41641 had an orbital companion. The same plot was repeated using other frequency components of the series of harmonics and no radial shift was detected in any case. Hence the low frequency harmonics are more likely caused by rotation than by an orbital companion.

As a final test to be able to definitely neglect binarity, spectral disentangling was conducted following the same procedure that was used by Kolbas et al. (2015). This method enables the separation of the individual spectra of the components of binary and multiple systems, along with the simultaneous determination of their orbital elements. In the case of HD 41641, no second spectrum was detected.

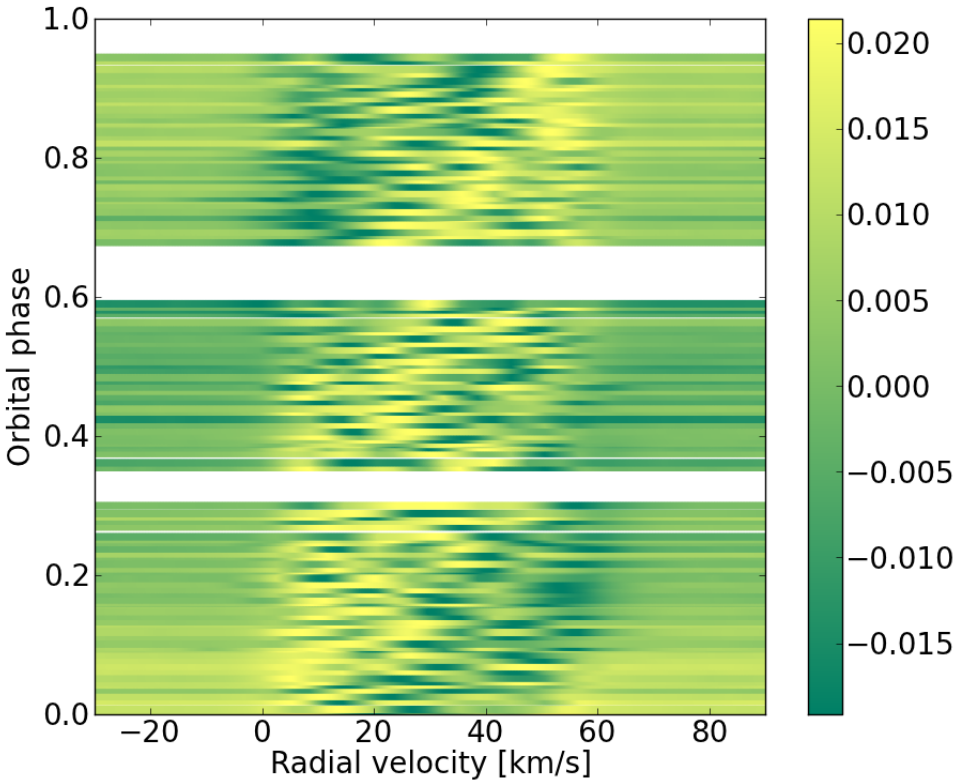

Figure 3.6: Color diagram of the relative flux after subtracting the mean profile of each LSD profile. They cover a period P = 1/F7.

3.4.2 Spots on the stellar surface

Following this line of argumentation, the presence of spots on the stellar surface creates line profile variations as well as the flux variations that were observed in the light curve (see Figure 2.7) and these changes are periodic with the rotation frequency. Because of its higher amplitude in the Fourier spectrum (see Figure 2.6) and its dominance in the PDM (see Figure 2.8) F7 was concluded to be rotation frequency although other components of the series of harmonics, specially F24, cannot be neglected. It is important to be sure that F7 has physical sense as rotation frequency and if any other of the peaks also does. Knowing the value of *vsini* and the fact that the equatorial velocity has to be higher than that, a lower limit for the radius of the star can be established for a given rotation frequency and compared with the obtained range.

$$v_{eq}\ [\text{in km/s}] = 2\pi R_* f_{rot} = 2\pi R_\odot \frac{R_*}{R_\odot} f_{rot} = 50.578 \frac{R_*}{R_\odot} f_{rot}[\ \text{in d}^{-1}], \tag{3.2}$$

$$v_{eq} > vsini = 30km/s \quad \Longrightarrow \quad \frac{R_*}{R_\odot} > \frac{30}{50.578F7} = 1.666, \tag{3.3}$$

where v_{eq} is the equatorial velocity, R_* is the stellar radius, f_{rot} is the rotation frequency and is equal to F7 in this particular case and $R_\odot$ is the radius of the Sun.

This illustrates that our assumption of F7 being a frequency caused by rotation is consistent. Note that all the other frequency members of the series of harmonics give meaningful lower limits too. In the particular case of F24, we obtain that R_* needs to be higher than $3.34R_\odot$ which is still possible according to the obtained radius range. On the other hand, if F50 is used, R_* is obtained to be higher than $42R_\odot$ and this is totally not compatible with the found range. F50, which was related with the amplitude variability of F4, is rejected as a possible rotation frequency.

Another test that can be used is related to the so-called critical velocity of rotation. If a star rotates at this velocity, the centrifugal acceleration exactly balances gravity. For it to be gravitationally stable, a star has to rotate clearly below this value so it can be used to establish an upper limit for the rotation frequency. The critical velocity of rotation v_{crit} can be computed as indicated by Equation 3.4,

$$v_{crit} = \sqrt{\frac{GM_*}{R_*}}, \tag{3.4}$$

where M_* and R_* are the mass and the radius of the star and G is the gravitational constant.

Using the expression obtained before for the equatorial velocity (Equation 3.2), the fraction of the critical velocity that the equatorial rotation velocity implies can be expressed as a function of the mass and the radius of a star as follows,

$$\frac{v_{eq}}{v_{crit}} = \frac{R_*^{1/2} 50.578 f_{rot} R_*/R_\odot}{(GM_*)^{1/2}} = 0.0412 \left(\frac{R_*}{R_\odot}\right)^{3/2} \left(\frac{M_*}{M_\odot}\right)^{-1/2}. \tag{3.5}$$

Substituting the estimated values for the radius and the mass of the star (see Section 3.3), i.e. $M_* = 2.3M_\odot$ and $R_* = 4.5R_\odot$, the equatorial velocity, assuming that F7 is the rotation frequency is about 26% of the critical one. As the uncertainties are large, it was checked that, even considering limiting cases, this fraction would still be less than 50%. This means that it is physically safe to affirm that F7 is the rotation velocity of HD 41641. Note that F24 is also physically meaningful so cannot be neglected.

An interesting point would be now to understand what is the cause of the spots. In order to check if they are caused by chemical inhomogeneities, an intensive study of the individual chemical abundances was performed with the previously described GSSP code and is summarized in the next section.

Study of the individual chemical abundances

As it was mentioned before, the GSSP code also allows to determine individual chemical abundances. The abundances of more than 50 chemical elements were fitted one by one with the code to the average spectrum. Each element was treated individually depending on the number of lines that it presents in the spectra. For example, for line-rich elements such as iron, the wavelength range used was the same that was used for the determination of the fundamental stellar parameters (4700 Å - 5700 Å). Additionally, the other four stellar parameters (i.e. $T_{\rm eff}$, $logg$, $vsini$ and ξ) were set free as iron has an important influence on them and fixing them would have introduced constraints to its abundance. On the other hand, for the analysis of elements with less spectral lines, the stellar parameters were set fixed and only small wavelength ranges where those lines are known to be present were fitted (e.g. in the the particular case or Magnesium the studied ranges were [4560.0Å - 4580.0Å], [4690.0Å - 4750.0Å] and [5150.0Å - 5190.0Å]).

The obtained abundances were compared with solar values (Asplund et al., 2009) and Table 3.3 summarizes the results. Only those elements whose abundances could be properly constrained are included in the table. The presented uncertainties were derived from the 1σ confidence level of the χ^2 minimization procedure.

Nine chemical elements, highlighted in blue in Table 3.3, showed, within the 1σ errorbars, different abundances than expected for a star of the derived global metallicity. For some of them the deviation is small taking the uncertainties into account (e.g. Mg, Ca or Ni) but some other present quite divergent values. The most remarkable ones are Oxygen, Manganese, Cobalt and Barium which show considerable overabundance and Zinc which was determined to be quite underabundant. Some other elements could be interesting (e.g. V and Zr) but it was impossible to reduce their uncertainties even working with different spectral ranges.

The detected peculiarities do not completely fit any classification of known chemically peculiar stars. HD 41641 is in the temperature range of Am stars and δ Sct pulsations have been already detected in several of these peculiar stars (Balona et al., 2015). However, although it presents underabundance of Sc as a Am star would present, the obtained iron abundance is completely normal while Am stars present strong overabundance of elements of the iron group.

As these chemical peculiarities could be related to a possible chemical character of the

Table 3.3: Chemical abundances of individual elements and comparison with solar values (Asplund et al., 2009).

Chemical Element	Abundance [E/H] [dex]	Expected ab.		Difference with solar
		Solar	[M/H]=-0.2	
C	-3.81 ± 0.2	-3.65	-3.85	-0.16 ± 0.2
O	-2.97 ± 0.21	-3.38	-3.58	+0.41 ± 0.21
Na	-6.09 ± 0.18	-5.87	-6.07	-0.21 ± 0.18
Mg	-4.52 ± 0.06	-4.51	-4.71	-0.01 ± 0.06
Si	-4.72 ± 0.26	-4.53	-4.73	-0.19 ± 0.26
Ca	-5.69 ± 0.09	-5.73	-5.93	+0.04 ± 0.09
Sc	-9.50 ± 0.39	-8.99	-9.19	-0.51 ± 0.39
Ti	-7.24 ± 0.16	-7.14	-7.34	-0.10 ± 0.16
V	$-7.71^{+0.36}_{-1.00}$	-8.04	-8.24	$+0.33^{+0.36}_{-1.00}$
Cr	-6.58 ± 0.14	-6.40	-6.60	-0.18 ± 0.14
Mn	-6.25 ± 0.08	-6.65	-6.85	+0.40 ± 0.08
Fe	-4.78 ± 0.08	-4.59	-4.79	-0.19 ± 0.08
Co	$-6.39^{+0.29}_{-0.45}$	-7.12	-7.32	$+0.73^{+0.29}_{-0.45}$
Ni	-6.28 ± 0.16	-5.81	-6.01	-0.47 ± 0.16
Zn	$-8.54^{+0.31}_{-0.69}$	-7.44	-7.64	$-1.10^{+0.31}_{-0.69}$
Y	-9.45 ± 0.17	-9.83	-10.03	+0.38 ± 0.17
Zr	-9.23 ± 0.5	-9.45	-9.65	+0.22 ± 0.5
Ba	-9.12 ± 0.14	-9.87	-10.07	+0.75 ± 0.14

spots, a deeper analysis was performed over these nine elements. If the irregular distribution of any of these chemical elements over the stellar surface is causing chemical spots, we would expect to detect variations on its chemical abundance over the phase. To study this effect, four individual spectra were selected to repeat the chemical analysis.

Using the LSD profiles introduced in Section 3.4.1 and shown in Figure 3.6, three profiles that present significant distortion in comparison with the mean profile and the one with the smallest distortion were chosen to be chemically analyzed. The spectra were phase-folded with the rotation period (P = 1/0.35603 days) and their phases were also taken into account to cover different orbital phases. Figure 3.7 shows the LSD profiles of the four selected spectra to show their distortion over the mean LSD profile. The least distorted profile is plotted in red while the highly distorted ones are plotted in black. The orbital phases and the number of the spectra are included in the plot.

The abundances of six of the nine elements, Mn, Co, Ni, Zn, Y and Ba, did not show

any variation with the phase within the obtained uncertainties but O, Mg and Ca may represent interesting cases and deserve a closer look. Table 3.4 lists the abundances of O, Mg and Ca obtained for the four studied spectra. For Oxygen, it can be seen that the detected overabundance in the average spectrum is enhanced at $\phi = 0.24$ and strongly reduced at $\phi = 0.60$ and 0.70. Magnesium and Calcium present a similar behavior. This

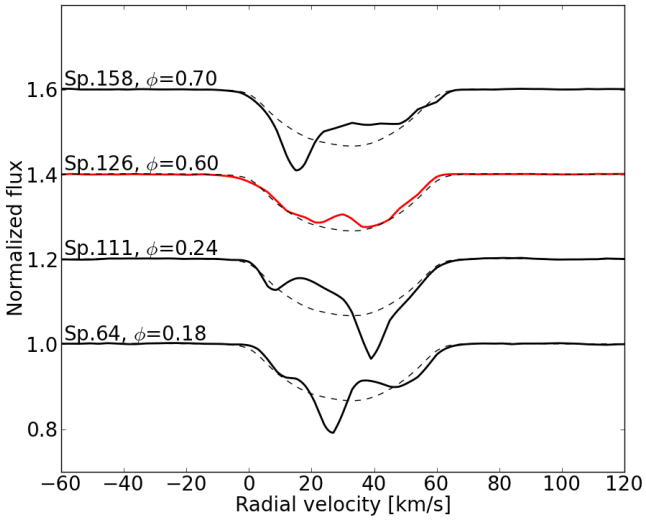

Figure 3.7: LSD profiles of the four spectra selected to analyze individual chemical abundances. Three of them present strong distortion (black) while the other one is the least distorted profile (red).

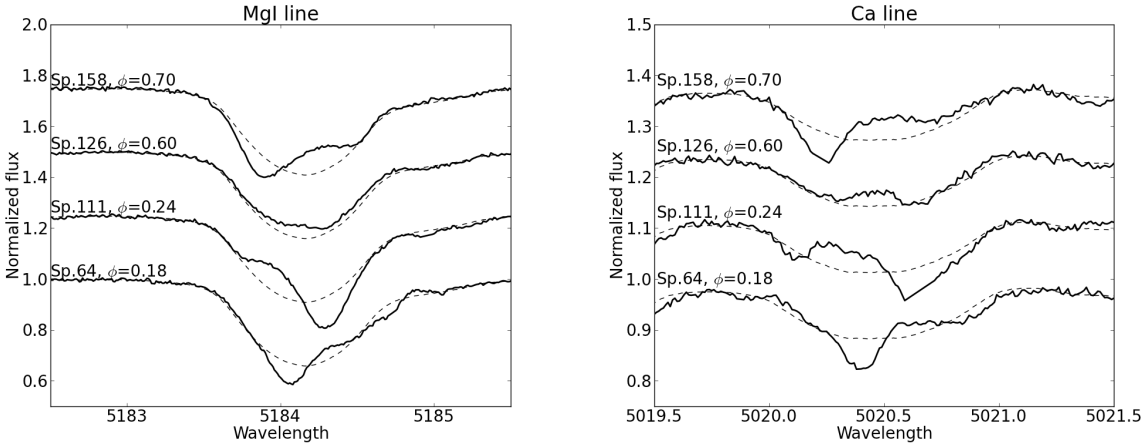

(a) (b)

Figure 3.8: Line profile variations with the rotation phase of a Magnesium (a) and a Calcium (b) lines.

Table 3.4: Variation with phase of the abundance of Oxygen, Magnesium and Calcium

O	**[O/H] [dex]**	**Difference (solar)**
Average	-2.97 ± 0.21	+0.41 ± 0.21
64; ϕ = 0.18	-3.04 ± 0.31	+0.34 ± 0.31
111; ϕ = 0.24	-2.61 ± 0.19	+0.77 ± 0.19
126; ϕ = 0.60	-3.26 ± 0.47	+0.12 ± 0.47
158; ϕ = 0.70	-3.39 ± 0.96	-0.01 ± 0.96
Mg	**[Mg/H] [dex]**	**Difference (solar)**
Average	-4.52 ± 0.06	-0.01 ± 0.06
64; ϕ = 0.18	-4.42 ± 0.09	+0.09 ± 0.09
111; ϕ = 0.24	-4.44 ± 0.13	+0.07 ± 0.13
126; ϕ = 0.60	-4.73 ± 0.08	-0.22 ± 0.08
158; ϕ = 0.70	-4.61 ± 0.10	-0.10 ± 0.10
Ca	**[Ca/H] [dex]**	**Difference (solar)**
Average	-5.69 ± 0.09	+0.04 ± 0.09
64; ϕ = 0.18	-5.52 ± 0.14	+0.21 ± 0.14
111; ϕ = 0.24	-5.53 ± 0.17	+0.20 ± 0.17
126; ϕ = 0.60	-5.80 ± 0.13	-0.07 ± 0.13
158; ϕ = 0.70	-5.84 ± 0.15	-0.11 ± 0.15

could be an evidence of chemical spots caused by an irregular distribution of some chemical elements over the surface but the uncertainties are large and it is difficult to draw a definite conclusion.

In Figure 3.8, the four studied spectra were used to graphically show the variability described in Table 3.4. A Magnesium line (a) and a Calcium line (b) were plotted for the four spectra to observe their phase-dependent line profile variability with respect to the mean profile of the line. Due to the smaller intensity of Oxygen lines, it was not easy to do the same plot for this element.

A more detailed study of the chemical abundances and their distribution is beyond the scope of this work but it would be very interesting to conduct it in the future.

3.5 Line profile variation and mode identification

As it was mentioned in the introduction, mode identification (-ID) is a crucial step in the study of an oscillating star. The line profile variations of several spectral lines were studied with the goal of identifying the excited modes in HD 41641. The moment method (Aerts, 1996) and the Fourier parameter fit (FPF) method (Zima, 2006) were used with this purpose. The main difference between both methods is that FPF relies on the Doppler broadening of the line profiles and uses the intensity information of each wavelength bin along the studied absorption line to look for periodicities while the moment method fits integrated n^{th} moments (i.e. the equivalent width (EW), the radial velocity (RV), the variance and the skewness) of the spectral line with theoretical values. The mathematical expression of the moments can be found in Equation (1.8).

The methods also have similarities. Both of them assume sinusoidal variations and neglect second order rotational effects. Depending on the target, one method may turn out to be more appropriate than the other one. The moment method is optimally suited for the analysis of slowly rotating stars that present pulsational modes up to a degree l of 4. On the other hand, the FPF method requires sufficient rotational broadening of the profile so it is more appropriate for faster rotators and high order modes can be identified with it.

Both approaches were used to analyze the spectral lines of HD 41641 in order to compare the obtained results but it was concluded that the moment method is more suitable for HD 41641 given its moderate rotation velocity of 30 ± 2 km/s (see Section 3.3). Our results are completely based on this method as from the FPF method only poorly constrained conclusions could be drawn. A complete mathematical description of the method is beyond the scope of this report but we refer to Aerts et al. (1992) and Aerts (1996) for it.

3.5.1 Line selection

A careful selection of the lines used for mode-ID is crucial. It is advisable to look for unblended deep and sharp lines with narrow wings in which the line profile variation is detectable across the whole profile and not only at the line center. For example it is a good advice to avoid hydrogen lines as they strongly suffer from Stark (pressure) broadening (Aerts et al., 2010).

In the case of HD 41641, the low projected rotational velocity results in quite narrow lines, which is an advantage and allows to have a lot of good candidate spectral lines to work with. Our mode-ID will be mainly based on the analysis of several iron lines across the whole spectrum. Table 3.5 gives a summary of the selected lines. Apart from the

Table 3.5: Spectral lines selected to study their profile variation and perform mode-ID.

	Central wavelength λ_0	**Element**
line 1	5367.467 Å	FeI
line 2	5383.369 Å	FeI
line 3	5393.168 Å	FeI
line 4	5362.869 Å	FeII
line 5	4508.288 Å	FeII
line 6	4549.479 Å	FeII
line 7	5237.32 Å	CrII
line 8	4779.985 Å	TiII
line 9	4786.531 Å	NiI

six selected iron lines, in order to have a more general picture, we decided to add to the list three other metal lines from elements different than iron. These were a chromium, a titanium and a nickel line. The regions around the nine spectral lines were carefully normalized by fitting the continuum to a linear spline function and prepared to be analyzed.

3.5.2 FAMIAS

The software used for the mode identification is called FAMIAS, acronym for Frequency Analysis and Mode Identification for Asteroseismology (Zima, 2008). It allows the analysis of photometric and spectroscopic data to search for periodicities and it is based on Fourier analysis techniques and least-squares fitting (LSF) algorithms to detected pulsation frequencies and identify the associated pulsation modes. The two mentioned methods, the moment method and the FPF method can be used when working with FAMIAS.

The 222 normalized line profiles were transformed from the wavelength domain to the radial velocity domain with FAMIAS by using the central wavelength of each feature (listed in Table 3.5). Also individual signal-to-noise ratios were computed for each profile and all of them were interpolated on a common dispersion grid and range. This last step needed to be done carefully because the wings of the spectral lines have to be totally inside the selected range for all the profiles but also not too much continuum should be included.

3.5.3 Extraction of oscillation frequencies

Although the analysis behind the moment method and the FPF method are different, the procedure carried out to search for the oscillation frequencies is quite similar for both and

it is also similar to the one described in Section 2.3.1 when working with PERIOD04 and the photometric data.

For each of the nine studied lines, the procedure is exactly the same. The Fourier spectrum of the data is computed in order to look for periodicities. In the case of the FPF method, the Fourier transform of the line profile is used while for the moment method, we work with the Fourier transform of each n^{th} moment independently. When a frequency peak has an amplitude higher than the significance level (S/N $>$ 4.0), a least-squares (LSF) is calculated to determine the amplitude and the phase. Then, that fit is prewhitened from the data and the new Fourier spectrum is computed to repeat the process until a frequency peak is found to have S/N $<$ 4.

Figure 3.9 shows the spectral window of the spectroscopic data set up to the Nyquist frequency as computed with FAMIAS (f_{Ny} = 23.588 d^{-1}). The daily alias peaks appear with an important amplitude, almost 90% of the amplitude for the first one and 50% for the second one. Hence, it is important to take this into account when we have to decide which oscillation frequencies are intrinsic from the star and independent. If this plot is compared with the spectral window of the photometric data set, which was presented in Figure 2.3(a), the difference between the relative amplitude of the alias peaks is impressive and shows again the benefits of working with space data. It is also important to notice that the Nyquist frequency is much lower now as the sampling of the data is much lower and also very irregular.

Figure 3.10 shows the Fourier spectra of the line profile and of the zeroth, first, second, third and fourth moments of the first studied FeI line (λ_0 = 5367.467 Å). The plots for

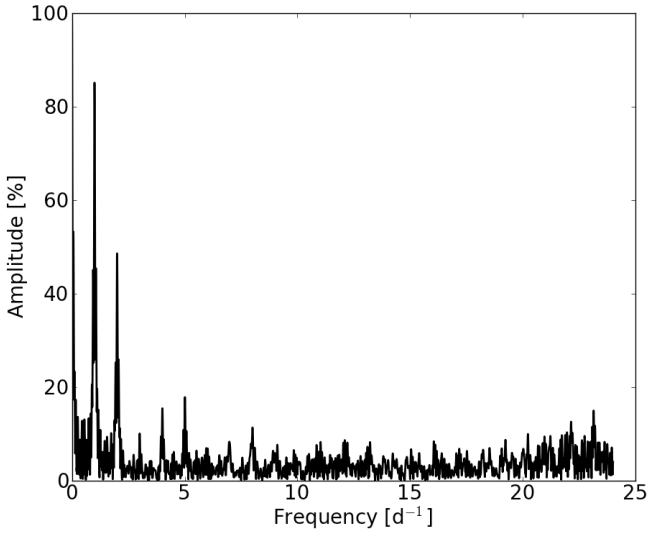

Figure 3.9: Spectral window of the spectroscopic data set.

the rest of the lines were not included as their behavior is similar. In the Fourier spectrum of the line profile, two groups of frequencies can be identified as it happened in the Fourier spectrum of the photometric data set (see figure 2.4). They are a group of peaks related to stellar rotation at lower frequencies and a group of p-mode oscillation frequencies between 10 and 20 d^{-1}. The third group of peaks that was observed before is outside the studied frequency range now ($> f_{Ny} = 23.588\ d^{-1}$). Looking at the spectra of the moments (see Figure 3.10), it can be observed how the low frequencies strongly dominate specially in the zeroth, first and third moments. This will complicate the identification of the oscillation modes. In Figure 3.11, the first and second moments of the nine studied line were phase-folded with the dominant frequency, F7, and plotted with blue dots. The red stars correspond to the best fit obtain with the mode identification (see Section 3.5.5).

The identified frequencies from the analysis of each moment and from the FPF method are listed in several tables in Appendix B together with their amplitudes and phases for each one of the nine analyzed lines. Their uncertainties were derived from the least-squares fitting algorithm. In the tables, it is also indicated when a frequency appeared also in the photometric analysis. It can be observed that often a frequency appears when using different moments. Those relations are listed in the last column of the tables.

If the first panel of figure 3.10 is compared with the other ones, it seems that the FPF method is more suitable for the target as the noise level of the first Fourier spectrum is lower. However, from the tables it is obvious that the moment method is more suitable

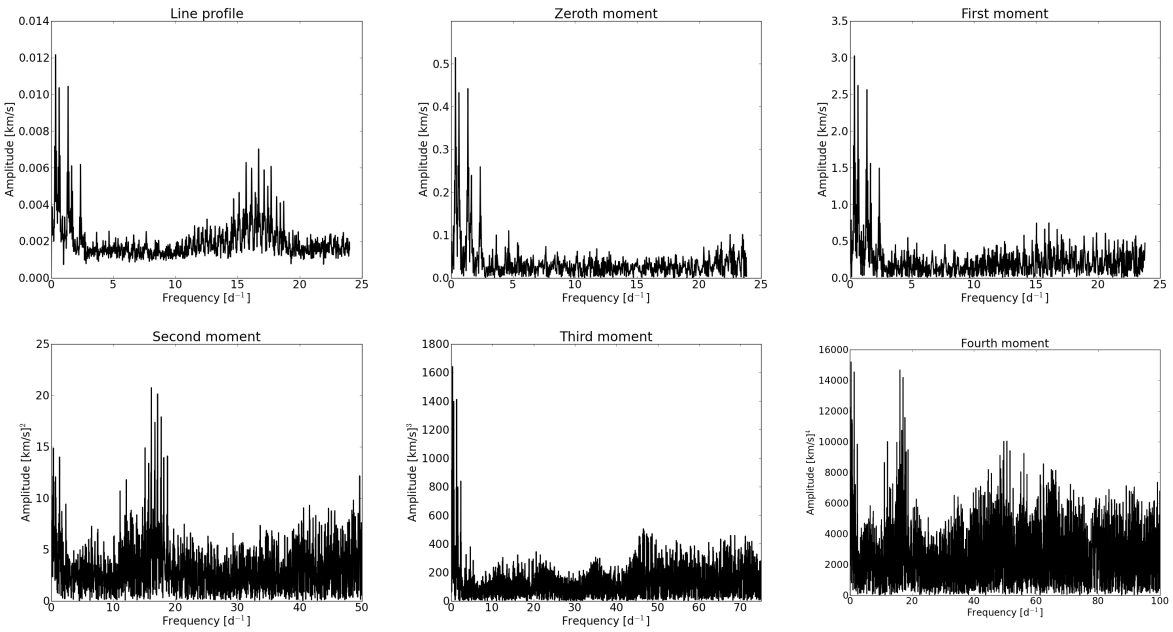

Figure 3.10: Fourier spectra of the line profile and of the moments of the first studied spectral line

to study HD 41641. In most of the analyzed lines, only one frequency was detected with the FPF method and this was the rotation frequency which is not associated to an oscillation mode. This is different only for line 6 (see Table B.6) where three frequencies were identified with S/N > 4. Mode-ID with the FPF method was impossible for eight of the nine selected spectral lines so the presented results are based on the moment method.

3.5.4 Frequency analysis

In total, 11 different frequencies were found. For the further discussion, the frequencies will be identified with the name that they received during the photometric analysis (i.e. a capital F and the number that received when they were ordered by amplitude). In

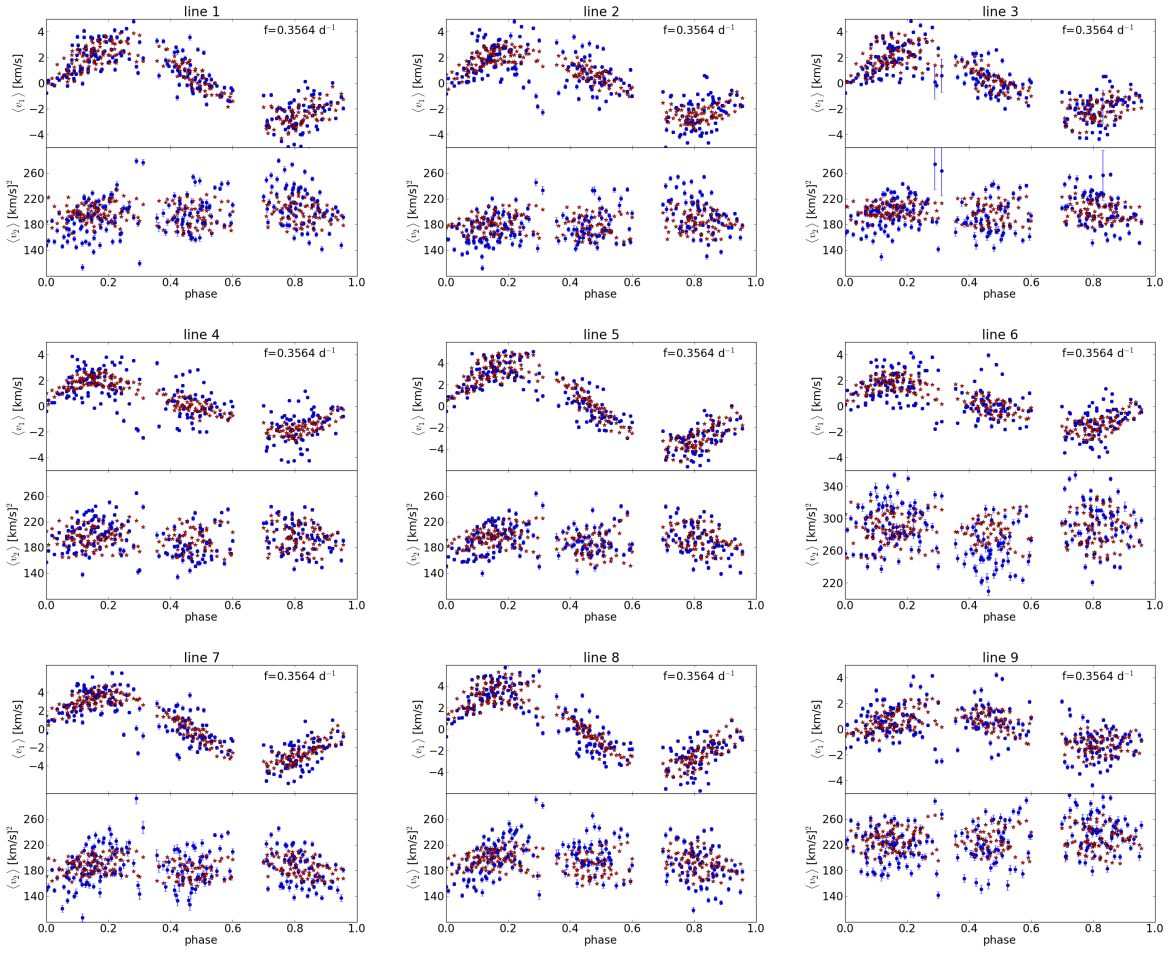

Figure 3.11: Phase plot (with F7 $= 0.35603$ d^{-1}) of the first and second moments of each studied line. The blue dots correspond to the moments as computed from the line profile and the red stars to the theoretical one obtained with the best fit.

the spectroscopic analysis with FAMIAS, the frequencies appear in different order for the different lines and not all of them are present in all the lines so, in order to be consistent, the notation that was used in Table A.1 remains here. In case that we need to refer to a frequency as it was obtained with FAMIAS a lowercase f will be used to avoid confusion. The tables in Appendix B include both notations.

Three of the 11 frequencies correspond to the one that was identified as the rotational frequency and two of its harmonics, F7, F19 (= 2*F7) and F24 (= F7/2). As it was mentioned, we find that F7 = 0.35603 d^{-1} strongly dominates the line profile variations. This frequency appears in all the lines and for all of them in most of the moments. Only for some lines, F7 is not present among the significant frequencies of the second and/or fourth moments.

Neglecting the three frequencies related to rotation and f = 0.03 $\pm$ 0.02 d^{-1} that appears twice (in lines 3 and 5) and was considered to be too small to be pulsation-related from this star, seven significant oscillation frequencies were identified. All of them but one (f = 14.448 $\pm$ 0.005 d^{-1} in lines 3 and 5) were also found in the photometric analysis. Note that the number of detected significant oscillation frequencies varies from one line to another.

3.5.5 Mode identification

The goal was to identify the quantum numbers l and m that characterize the oscillation mode that are excited and relate to each one of the identified frequencies. During this final part of the analysis, the results from the LSF are imported and combined with physical stellar parameters. All the different identified frequencies have to be included in this last LSF that will be computed to fit the theoretical moments. Frequencies caused by combinations of other frequencies and frequency harmonics are included as their influence needs to be pre-whitened too.

There are three types of parameters that play a role in the mode-ID. First of all, the stellar parameters. Some of them need to be fixed while some others can freely vary inside a given range to optimize the fitting with FAMIAS. A mass range between 1.5 and 3.0 $M_\odot$ and a radius range between 2 and 7 $R_\odot$ were established as they were estimated from the fundamental parameters in Section 3.3. $T_{\rm eff}$, $logg$ and the metallicity [M/H] cannot be set as free variables so the values previously presented in Table 3.2 were used. Finally a wide range of inclination angles from 5^o to 85^o was defined and the $vsini$ was set as variable within an interval around the obtained value of 30 km/s (i.e. from 20 to 40 km/s).

The second set of parameters are line profile related. Some of them are known, as the central wavelength or the individual S/N ratio of each spectrum which was computed before, and the other ones can also be constrained with FAMIAS. These are pulsation-

ally independent parameters and can be determine from a fit of a rotationally broadened synthetic line profile together with the *vsini*.

Finally, the pulsation mode parameters: the degree (l), the order (m), the velocity amplitude and the phase of each studied pulsation frequency. The initial range of the degree was established from $l = 0$ to $l = 4$ and the range of the order from m = -4 to $m = +4$. The velocity amplitude was initially give a wide range from 0 km/s to 30 km/s and the phase was given two different values: the one obtained from the LSF and the one separated from this by half a phase.

After reducing the range of the *vsini* and the line profile related parameters during the first iterations, the pulsation mode parameters were slowly and carefully constrained in an iterative process. The rest of the stellar parameters were not constrained. All the intrinsic and independent frequencies identified as significant (S/N $>$ 4.0) for a line, independently of which moment they appeared in, were included in the fitting at the same time. Table 3.6 summarizes the results obtained by means of the described procedure.

The obtained χ^2 values were quite high in general so the presented results correspond with the combination of l and m that gave the minimum even if it still was relatively high. As a general procedure, a value of l or m associated to a given frequency was neglected when together with the best combination of all the other quantum numbers gave a χ^2 value higher than the obtained minimum χ^2 of that run plus one. Initially the most clearly disposable options were neglected and each l and m was slowly constrained. When two or more values gave a very close χ^2 result, all of them were considered and included in Table 3.6 as possible solutions.

A generalized effect that was encountered when dealing with every single line is that the rotation frequency dominated so much over the behavior of the line moments that it was impossible to get a decent fit without taking it into account in the mode ID procedure. It is clear that it makes no sense to relate an oscillation mode to a frequency that was identified as a rotation frequency but it was necessary to include F7 = 0.35603 d^{-1} to constrain the rest of the modes.

Figure 3.11 included the first and second moments of each line phase-folded with the strongly dominant rotation frequency F7 = 0.35603 d^{-1}. From the plots it can be observed that the fit is far from optimal. It was difficult in general to create clear constraints on the quantum numbers.

From the Table 3.6, some conclusions can be drawn:

- Frequency F1 appears in seven of the nine lines and the wave was identified as a nonradial prograde mode (i.e. the wave travels in the direction of the stellar rotation)

Table 3.6: Results of the mode identification with FAMIAS

	F1=17.69	**F5=16.03**	**F6=16.69**	**F15=12.08**	**F40=16.11**	**f=14.45**
line 1	l = 2 m = 2	l = 1, 2 m = -1		l = 3 m = 1, 3	Impossible to constrain	
line 2	l = 2 m = 1			l = 3 m = -3		
line 3		l = 1, 2 m = -1	l = 2 m = 2		Impossible to constrain	l = 1 m = -1, 0
line 4	l = 2 m = 2				l = 3, 4 m = -3	
line 5	l = 2, 3 m = 2	l = 1, 2 m = -1	l = 2 m = 2		l = 3, 4 m = -3	l = 0, 1 m = 0
line 6			l = 1, 2 m = 1		l = 3, 4 m = -3	
line 7	l = 3 m = 2				Impossible to constrain	
line 8	l = 3 m = 1	l = 1, 2 m = -1	l = 1, 2 m = 1		Impossible to constrain	
line 9	l = 1, 2 m = 1		l = 1, 2, 3 m = 1		l = 3, 4 m = 2, 3, 4	

in all the cases. l is likely 2 or 3 and m is 1 or 2. All the different combinations were obtained in one line or another.

- Frequency F5 appears in four lines and the same result is constrained for all of them: l = 1 or 2 and m = -1. It was impossible to distinguish between the two possible degrees in the four cases.

- Frequency F6 appears in five lines in all of them is identified as a prograde mode with l = 1, 2 or 3 and m = 1 or 2. l = 3 was only obtained for the last line, the NiI line, for which this frequency was especially difficult to constrain in comparison with the other lines.

- Frequency F15 was only identified among the significant frequencies in the first two iron lines and the MI was ambiguous: l = 3 and m = 1 or 3 in line 1 and l = 3 and m = -3 in line 2. In contrast with the previous cases, even the direction of propagation is difficult to know for this frequency.

- Frequency F40 was a particularly difficult case. It was impossible to draw any conclusion from the MI of most of the lines where it was present. Those lines from whose analysis some constrains were possible suggest that it is a high degree

mode and more likely retrograde. Note that again from line 9 something different is concluded and F40 is identified as prograde.

- Frequency f=14.45 only appears in two of the iron lines. It was identified as a low degree mode from line 3 and as a radial mode from line 5.

3.6 Inclination angle

Finally, it was mentioned that spectroscopic mode identification could also be used to determine the inclination angle. During the mode identification, the inclination had been set as a variable parameter in its complete possible range. After the determination of

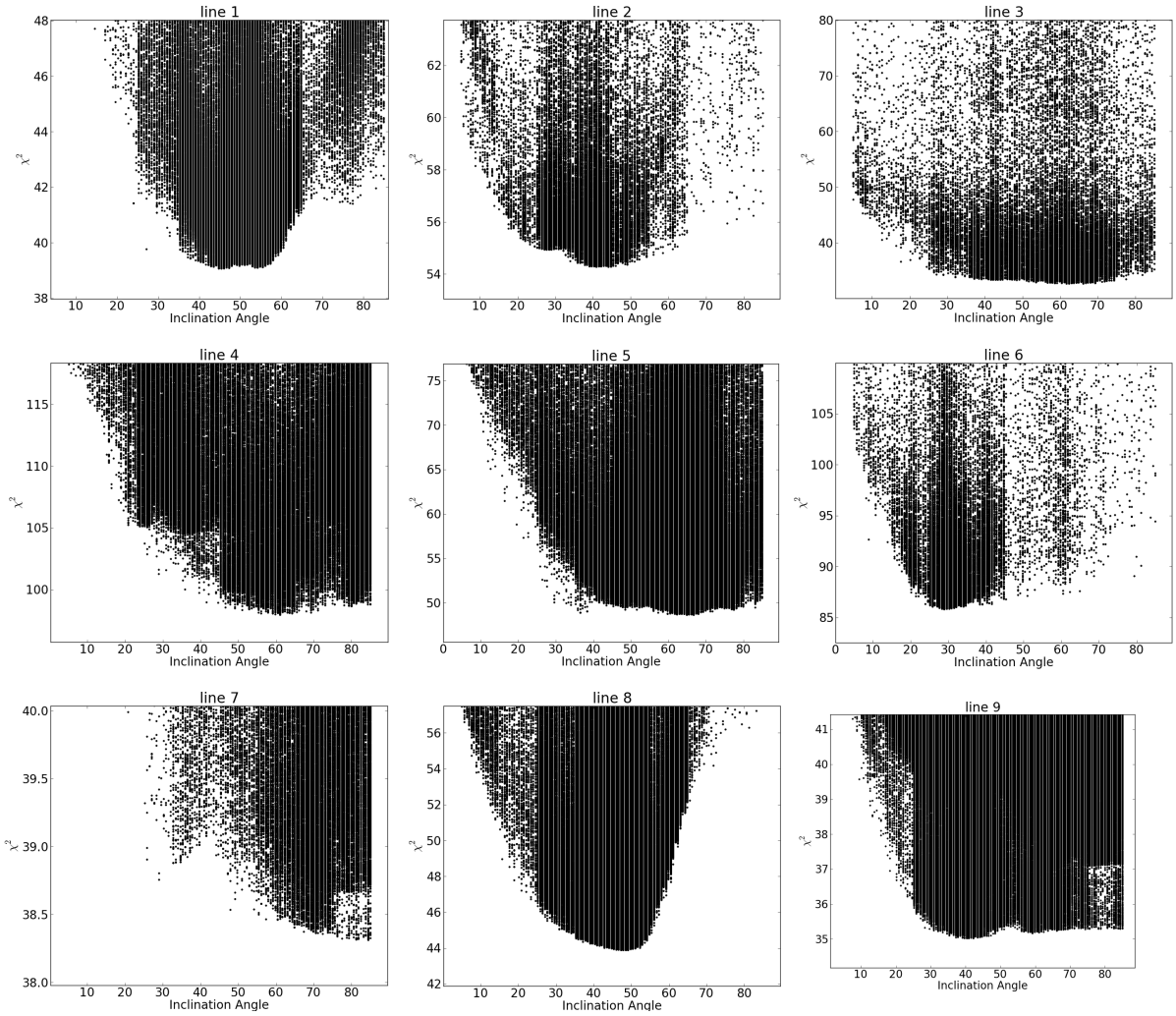

Figure 3.12: χ^2 values of the models as a function of the inclination angle for the nine studied lines.

the best (l, m) combinations, we attempted to put some constraints on it. The two or three combinations of the quantum numbers of each frequency that had given the best χ^2 values were set free as well as the inclination and a grid search over all the combinations of parameters was conducted. Figure 3.12 shows the χ^2 values obtained for the inclination angle during this last run but it is very difficult to conclude something from this plots.

Using the relation between the equatorial and the projected rotational velocities (Equation 3.2) and the estimated radius range, constraints on the inclination angle could also be set. However, the uncertainties on the radius are quite large and it is not sure if either F7 or F24 is the rotation frequency, as both of them are physically meaningful. This leads to a range for the inclination angle that covers almost all the possibilities as the plots do.

Chapter 4

Summary of results and conclusions

We carried out an intense asteroseismic study of the δ Sct star HD 41641. This was based on two different data sets that had been simultaneously obtained: a 94-day-long photometric data set obtained with the CoRoT space telescope between December, 2010 and March, 2011 and 222 high-resolution spectra obtained with the HARPS high-resolution spectrograph to complement CoRoT observations between December 23, 2010 and January 12, 2011.

The photometric data was first analyzed and some interesting results were obtained from it. The frequency analysis performed on the CoRoT light curve revealed a total of 90 frequencies with S/N over the chosen significance threshold (S/N $>$ 4.0). All of them were detected in a range between 0 and 40 d^{-1} and were distributed in three groups of frequencies.

The group of peaks detected at the lowest frequency domain was found between 0 and 1 d^{-1}. They have been concluded not to be oscillation frequencies but to be associated to another physical mechanism, either binarity or spots on the stellar surface. The main reasoning to reject them as pulsation frequencies was the complete harmonic series that they conformed. Several tests were conducted to decide which one of the low frequency peaks was really related to one of these physical mechanisms and F7 = 0.35603 $\pm$ 0.00001 d^{-1} was suggested to likely be the one. To distinguish between the presence of an orbital companion or the presence of spots on the surface as the cause of the low frequency peaks, it was necessary to include the spectroscopic analysis. We could not find any evidence of binarity. No Doppler shift was detected studying the line profile variation and the spectral disentangling technique did not show the presence of two objects either. Hence, these peaks were concluded to be caused by spots that cause brightness and line profile variations with the rotation phase. In order to determine if the nature of the spots was chemical, a complete chemical analysis was performed and the individual abundances of more than 50 elements were studied. Several interesting chemical peculiarities were detected and also variation of those with the phase of F7 suggesting that the spots appear in a complex distribution of some chemical elements over the stellar surface. It would

be interesting to further analyze the observed peculiarities and their variation with the rotation phase.

The other two groups of peaks found in the photometric analysis are within the expected p-mode frequency range for a δ Sct star. All the peaks identified in the group with higher frequencies were concluded to be combination peaks and not independent oscillation frequencies of the star. Hence, the independent p-mode oscillation frequencies of HD 41641 lie between 10 and 20 d^{-1}. Some relations could be found between several of those peaks but the high density of the spectrum complicated its analysis. The amplitude and frequency variability of the eight dominant frequencies were studied dividing the photometric data set into ten subsets. The amplitudes of seven of the frequencies were stable or only slightly unstable in time but F4 was observed to be a very interesting case. It presented strong amplitude variability that seemed to be periodic with a period of about 72 days. This periodicity could be detected in the Fourier spectrum as a frequency peak of 0.013955 ± 0.000008 d^{-1}.

The spectroscopic data was used to derive the fundamental stellar parameters of HD 41641. The star was determined to have an effective temperature of 7200 K, a surface gravity of 3.5 dex, a metallicity of -0.2 dex compared to solar and to rotate with a projected velocity of 30 km/s. Also the microturbulent velocity was determined to be $\xi = 1.0$ km/s. These values allowed to also estimate the position of the target in the HR diagram and hence to put some constraints on the mass and the radius of the target.

Finally, a frequency analysis was also conducted over the spectroscopic data set and this was done with FAMIAS. Periodicities were searched over nine metal line profiles and their integrated moments and most of the found frequencies had been detected also during the photometric analysis. Much less frequencies were found and a clear dominance of the low frequencies complicated the mode identification. Only a few constraints could be set for some of the detected oscillation modes.

To sum up, HD 41641 was physically and asteroseismically described for the first time. Most of the questions that we addressed about its oscillation frequencies and amplitudes were answered. The identification of the oscillation modes was not as successful but constraints were established and a different approach will be conducted to verify our results in light of a future publication. Other effects such us rotation and chemical peculiarities were also described. Concerning the second one, further analysis would be advisable and Doppler Imaging (e.g. Kochukhov 2004) is another of our future prospects. Theoretical modeling was beyond the scope of our initial goals as we wanted to focus on an observational description. It was not addressed for this master thesis but this report might be used in a near future as reference for a more theoretical work as it represents a quite complete description of a δ Sct star.

Finally, as a general remark and maybe more as personal conclusion, I would like to

suggest the necessity of having a general catalog or a review paper with the compilation of the obtained information about δ Sct stars from data analysis. The most complete catalog about these targets was done by Rodríguez & Breger (2001) but years before the space missions MOST, CoRoT and Kepler. After the publication of Rodríguez & Breger (2001), hundreds of confirmed δ Sct stars have been published and a compilation of their study would be really useful for further evolutionary studies (e.g., the comparison to pre-MS δ Sct stars done by Zwintz et al. 2014).

Appendix A

Frequencies from photometry

Table A.1: Frequencies found in the photometric data set with Period04

	Freq [d^{-1}]	**Ampl ± 5**	**Phase**	**Relation**
F1	17.702586(6)	5592	0.2270(1)	
F2	15.015649(7)	4627	0.7607(2)	
F3	16.381735(7)	4552	0.8344(2)	
F4	15.165792(7)	4482	0.1690(2)	
F5	16.037797(8)	4010	0.1457(2)	
F6	16.688825(8)	3922	0.4959(2)	
F7	0.35603(1)	3001	0.9103(3)	
F8	13.00610(1)	3049	0.9942(3)	
F9	14.85454(1)	2816	0.2653(3)	
F10	14.51090(1)	2390	0.9283(4)	
F11	15.15259(1)	2091	0.6876(4)	
F12	11.79415(1)	2087	0.1209(4)	
F13	13.77507(2)	1941	0.2155(4)	
F14	12.49191(2)	1878	0.1244(4)	
F15	12.08211(2)	1845	0.1165(5)	
F16	13.08583(2)	1799	0.8731(5)	
F17	13.45051(2)	1699	0.0724(5)	
F18	16.21431(2)	1670	0.1218(5)	
F19	0.71244(2)	1572	0.0233(5)	2 * $F7^{10}$
F20	12.65273(2)	1407	0.1650(6)	
F21	11.46569(3)	910	0.0130(9)	
F22	13.61648(3)	969	0.4143(9)	
F23	17.12048(3)	941	0.9135(9)	
F24	0.177556(3)	953	0.5607(9)	(1/2) * $F7^{10}$
F25	15.45448(3)	916	0.7549(9)	
F26	13.27223(5)	664	0.899(1)	
F27	13.40596(5)	641	0.800(1)	
F28	16.67089(5)	598	0.903(1)	

F29	16.53971(5)	531	0.451(2)	
F30	15.17520(5)	573	0.047(1)	
F31	15.51908(6)	496	0.223(2)	
F32	17.42123(6)	509	0.409(2)	
F33	12.55862(6)	520	0.487(2)	
F34	16.77657(6)	477	0.120(2)	
F35	10.26628(7)	461	0.216(2)	
F36	0.53421(7)	466	0.694(2)	(3/2) * $F7^{10}$
F37	11.87972(7)	450	0.686(2)	
F38	14.81871(7)	464	0.012(2)	F30 - $F7^{10}$
F39	16.05378(7)	470	0.849(2)	F31 + $F36^{10}$
F40	16.11973(7)	453	0.328(2)	
F41	17.39141(7)	439	0.411(2)	
F42	33.74053(7)	435	0.701(2)	F5 + F7 + $F82^3$
F43	11.94340(8)	410	0.276(2)	
F44	15.96681(7)	436	0.602(2)	F41 - 4*$F7^5$
F45	31.62962(8)	410	0.149(2)	F36 + F81 + $F81^3$
F46	11.63531(8)	393	0.040(2)	
F47	11.47962(8)	410	0.191(2)	
F48	15.31141(8)	384	0.838(2)	
F49	13.19819(8)	379	0.032(2)	
F50	0.013955(8)	394	0.919(2)	
F51	15.28035(9)	360	0.501(2)	
F52	12.86410(8)	371	0.481(2)	
F53	15.79213(9)	344	0.504(2)	
F54	15.13658(9)	352	0.869(2)	
F55	16.50175(9)	336	0.709(2)	F44 + $F36^{10}$
F56	12.54156(9)	345	0.403(2)	
F57	31.5340(1)	303	0.998(3)	F9 + F19 + $F44^3$
F58	16.9502(1)	308	0.095(3)	
F59	33.1568(1)	261	0.939(3)	F34 + F48 + $F62^3$
F60	18.8593(1)	305	0.816(3)	
F61	11.6100(1)	308	0.234(3)	
F62	1.0685(1)	292	0.996(3)	3 * $F7^{10}$
F63	31.9568(1)	290	0.935(3)	F7 + F39 + $F81^{10}$
F64	31.3315(1)	300	0.490(3)	F27 + F36 + $F41^3$
F65	12.5194(1)	296	0.880(3)	
F66	31.4279(1)	287	0.602(3)	F7 + F51 + $F53^{10}$
F67	14.6914(1)	280	0.619(3)	
F68	12.7153(1)	262	0.099(3)	
F69	12.4275(1)	267	0.785(3)	
F70	29.7699(1)	270	0.365(3)	F5 + F36 + $F49^3$
F71	14.6385(1)	274	0.013(3)	
F72	12.3964(1)	257	0.573(3)	
F73	15.4837(1)	249	0.457(3)	
F74	17.4802(1)	254	0.061(3)	

F75	10.5899(1)	243	0.174(3)	F47 - F19 - F24[5]
F76	32.4055(1)	241	0.897(3)	F3 + F19 + F48[1]
F77	31.2486(1)	238	0.095(4)	F3 + F7 + F10[1]
F78	12.7454(1)	242	0.830(3)	
F79	33.1738(1)	245	0.582(3)	F23 + F31 + F36[1]
F80	31.4874(1)	235	0.573(4)	F24 + F28 + F71[5]
F81	15.5477(1)	232	0.507(4)	F2 + F36[10]
F82	17.3465(1)	228	0.189(4)	F1 - F7[1]
F83	28.9778(1)	223	0.178(4)	F7 + F15 + F29[1]
F84	12.93642(6)	474	0.495(2)	
F85	12.93647(7)	419	0.690(2)	
F86	14.2609(1)	213	0.817(4)	
F87	16.3299(1)	210	0.142(4)	
F88	30.1591(1)	209	0.881(4)	F6 + F36 + F84[5]
F89	15.8110(1)	211	0.453(4)	F25 + F7[5]
F90	12.0681(2)	136	0.826(6)	

Appendix B

Frequencies from spectroscopy

Table B.1: line1: FeI, λ_0 = 5367.467 Å

fi	Freq [d^{-1}]	Amplitude	Phase	Relations
Zeroth moment (Equivalent Width) [km/s]				
f1 = F7	0.3564(4)	0.545(9)	0.328(2)	
f2 = F24	0.175(3)	0.073(8)	0.61(2)	= f1/2
First moment (Centroid velocity variations) [km/s]				
f3 = F7	0.3579(7)	2.85(8)	0.607(4)	= f1
f4 = F5	16.032(3)	0.71(8)	0.06(2)	
Second moment (Width variations) [$(km/s)^2$]				
f5 = F40	16.111(2)	21(2)	0.10(1)	
f6 = F1	17.698(2)	17(2)	0.65(2)	
f7 = F7	0.353(3)	17(2)	0.86(2)	= f1
f8 = F19	0.716(3)	13(2)	0.98(3)	= 2*f1
Third moment (Skewness variations) [$(km/s)^3$]				
f9 = F7	0.358(1)	1510(50)	0.608(6)	= f1
f10	0.469(9)	260(50)	0.65(4)	
Fourth moment [$(km/s)^4$]				
f11 = F7	0.361(2)	17000(1000)	0.30(1)	= f1
f12 = F40	16.111(2)	14000(1000)	0.27(1)	= f5
f13 = F1	17.700(3)	12000(1000)	0.14(1)	= f6
f14 = F19	0.721(4)	10000(1000)	0.70(2)	= 2*f1
f15 = F15	12.087(3)	8000(1000)	0.23(2)	
f16 = F3	16.385(4)	8000(1000)	0.64(3)	= f1+f4
f17 = F24	0.181(5)	7000(1000)	0.01(3)	= f1/2
FPF method [km/s]				
f18 = F7	0.358	0.9(1)		= f1

Table B.2: line2: FeI, λ_0 = 5383.369 Å

fi	Freq [d^{-1}]	Amplitude	Phase	Relations
Zeroth moment (Equivalent Width) [km/s]				
f1 = F7	0.3577(8)	0.74(3)	0.454(5)	
First moment (Centroid velocity variations) [km/s]				
f2 = F7	0.358(1)	2.5(1)	0.596(7)	= f1
Second moment (Width variations [$(km/s)^2$]				
f3 = F40	16.114(2)	18(2)	0.74(1)	
f4 = F7	0.353(2)	16(2)	0.80(2)	= f1
f5 = F1	17.698(3)	15(2)	0.64(2)	
f6 = F19	0.708(3)	12(2)	0.98(2)	= 2*f1
Third moment (Skewness variations) [$(km/s)^3$]				
f7 = F7	0.358(1)	1520(50)	0.595(7)	= f1
Fourth moment [$(km/s)^4$]				
f8 = F7	0.353(2)	14000(1000)	0.74(2)	= f1
f9 = F40	16.111(2)	11000(1000)	0.03(2)	= f3
f10 = F1	17.703(3)	9000(1000)	0.99(2)	= f5
f11 = F19	0.711(4)	9000(1000)	0.63(3)	= 2*f1
FPF method [km/s]				
f12 = F7	0.358	1.1(1)		= f1

Table B.3: line3: FeI, λ_0 = 5393.168 Å

fi	Freq [d^{-1}]	Amplitude	Phase	Relations
Zeroth moment (Equivalent Width) [km/s]				
f1 = F7	0.3579(6)	0.47(1)	0.883(3)	
First moment (Centroid velocity variations) [km/s]				
f2 = F7	0.3579(6)	2.47(5)	0.639(4)	= f1
f3 = F5	16.032(4)	0.61(5)	0.04(1)	
f4 = F6	16.698(7)	0.61(5)	0.11(1)	
f5	0.029(3)	0.53(7)	0.13(2)	
f6	14.448(5)	0.48(5)	0.99(2)	
f7 = F24	0.173(6)	0.34(6)	0.70(3)	= f1/2
Second moment (Width variations) [$(km/s)^2$]				
f8 = F40	16.114(3)	18(1)	0.67(1)	
f9 = F6	16.694(5)	14(1)	0.45(2)	= f4
f10 = F19	0.713(3)	12(1)	0.29(2)	= 2*f1
Third moment (Skewness variations) [$(km/s)^3$]				
f11 = F7	0.356(2)	1140(40)	0.965(6)	= f1
f12	0.03(2)	270(40)	0.13(3)	= f5
Fourth moment [$(km/s)^4$]				
f13 = F40	16.111(3)	10000(1000)	0.01(2)	= f8
FPF method [km/s]				
f14 = F7	0.358	0.72(8)		= f1

Table B.4: line4: FeII, λ_0 = 5362.869 Å

fi	Freq [d^{-1}]	Amplitude	Phase	Relations
Zeroth moment (Equivalent Width) [km/s]				
f1 = F7	0.3585(7)	0.84(3)	0.474(5)	
First moment (Centroid velocity variations) [km/s]				
f2 = F7	0.355(1)	1.9(1)	0.950(1)	= f1
Second moment (Width variations) [$(km/s)^2$]				
f3 = F40	16.116(2)	18(1)	0.36(1)	
f4 = F1	17.696(2)	15(1)	0.98(1)	
f5 = F19	0.708(2)	14(1)	0.02(1)	= 2*f1
Third moment (Skewness variations) [$(km/s)^3$]				
f6 = F7	0.355(1)	890(50)	0.889(9)	= f1
Fourth moment [$(km/s)^4$]				
f7 = F40	16.114(2)	10000(1000)	0.69(1)	= f3
f8 = F19	0.708(3)	9000(1000)	0.01(2)	= 2*f1
f9 = F1	17.699(3)	9000(1000)	0.65(2)	= f4
FPF method [km/s]				
f10 = F7	0.358	1.1(1)		= f1

Table B.5: line5: FeII, λ_0 = 4508.288 Å

fi	Freq [d^{-1}]	Amplitude	Phase	Relations
Zeroth moment (Equivalent Width) [km/s]				
f1 = F7	0.3576(4)	1.76(3)	0.726(3)	
First moment (Centroid velocity variations) [km/s]				
f2 = F7	0.3554(5)	3.76(7)	0.941(3)	= f1
f3 = F5	16.035(2)	0.65(7)	0.72(2)	
f4 = F6	16.698(3)	0.61(7)	0.10(2)	
f5	0.03(1)	0.44(7)	0.99(4)	
f6	14.450(3)	0.50(7)	0.64(2)	
Second moment (Width variations) [$(km/s)^2$]				
f7 = F1	17.693(3)	14(2)	0.30(2)	
f8 = F40	16.111(3)	13(2)	0.99(2)	
Third moment (Skewness variations) [$(km/s)^3$]				
f9 = F7	0.3554(7)	1690(50)	0.949(5)	= f1
Fourth moment [$(km/s)^4$]				
FPF method [km/s]				
f10 = F7	0.358	2.5(1)		= f1

Table B.6: line6: FeII, λ_0 = 4549.479 Å

fi	Freq [d^{-1}]	Amplitude	Phase	Relations
Zeroth moment (Equivalent Width) [km/s]				
f1 = F7	0.3580(4)	2.96(5)	0.327(3)	
f2 = F24	0.180(5)	0.31(5)	0.85(3)	= f1/2
First moment (Centroid velocity variations) [km/s]				
f3 = F7	0.355(1)	1.84(9)	0.949(9)	= f1
Second moment (Width variations) [$(km/s)^2$]				
f4 = F40	16.111(2)	19(2)	0.02(1)	
f5 = F6	16.684(2)	17(2)	0.81(2)	
f6 = F19	0.708(2)	17(2)	0.98(1)	= 2*f1
Third moment (Skewness variations) [$(km/s)^3$]				
f7 = F7	0.358(1)	1360(70)	0.638(9)	= f1
Fourth moment [$(km/s)^4$]				
f8 = F6	16.681(3)	21000(2000)	0.17(2)	= f5
f9 = F19	0.708(4)	21000(3000)	0.01(2)	= 2*f1
f10 = F40	16.113(2)	23000(2000)	0.69(2)	= f4
f11 = F7	0.360(7)	13000(3000)	0.03(3)	= f1
FPF method [km/s]				
f12 = F7	0.360	3.5(2)		= f1
f8 = F6	16.686	1.2(2)		= f5
f10 = F40	16.109	1.0(2)		= f4

Table B.7: line7: CrII, $\lambda_0 = 5237.32$ Å

fi	Freq [d^{-1}]	Amplitude	Phase	Relations
Zeroth moment (Equivalent Width) [km/s]				
f1 = F7	0.3578(7)	0.84(3)	0.273(5)	
First moment (Centroid velocity variations) [km/s]				
f2 = F7	0.3559(9)	3.6(1)	0.753(6)	= f1
Second moment (Width variations) [$(km/s)^2$]				
f3 = F1	17.699(3)	17(2)	0.06(2)	
f4 = F40	16.114(3)	16(2)	0.07(2)	
Third moment (Skewness variations) [$(km/s)^3$]				
f5 = F7	0.3554(9)	1460(50)	0.965(6)	= f1
Fourth moment [$(km/s)^4$]				
f6 = F1	17.701(3)	10000(1000)	0.20(2)	= f3
f7 = F40	16.113(3)	9000(1000)	0.28(2)	= f4
FPF method [km/s]				
f8 = F7	0.358	1.26(9)		= f1

Table B.8: line8: TiII, $\lambda_0 = 4779.985$ Å

fi	Freq [d^{-1}]	Amplitude	Phase	Relations
Zeroth moment (Equivalent Width) [km/s]				
f1 = F7	0.3571(5)	0.98(2)	0.623(3)	
First moment (Centroid velocity variations) [km/s]				
f2 = F7	0.3554(7)	3.65(9)	0.957(4)	= f1
f3 = F5	16.032(3)	0.94(9)	0.07(2)	
Second moment (Width variations) [$(km/s)^2$]				
f4 = F40	16.111(3)	18(2)	0.02(2)	
f5 = F1	17.696(3)	17(2)	0.98(2)	
Third moment (Skewness variations) [$(km/s)^3$]				
f6 = F7	0.355(1)	1520(60)	0.958(6)	= f1
Fourth moment [$(km/s)^4$]				
f7 = F40	16.106(3)	11000(1000)	0.65(2)	= f4
f8 = F7	0.368(3)	10000(1000)	0.16(2)	= f1
f9 = F6	16.694(3)	9000(1000)	0.49(2)	
FPF method [km/s]				
f10 = F7	0.358	1.5(1)		= f1

Table B.9: line9: NiI, $\lambda_0 = 4786.531$ Å

fi	Freq [d^{-1}]	Amplitude	Phase	Relations
Zeroth moment (Equivalent Width) [km/s]				
f1 = F7	0.360(3)	0.24(3)	0.48(2)	
First moment (Centroid velocity variations) [km/s]				
f2 = F7	0.358(2)	1.29(9)	0.54(1)	= f1
f3 = F1	17.696(3)	0.9(1)	0.29(2)	
Second moment (Width variations) [$(km/s)^2$]				
f4 = F40	16.114(2)	18(2)	0.69(1)	
f5 = F6	16.694(3)	18(2)	0.84(2)	
f6 = F7	0.358(3)	14(2)	0.09(2)	= f1
Third moment (Skewness variations) [$(km/s)^3$]				
f7 = F7	0.355(3)	840(60)	0.94(1)	= f1
f8 = F1	17.700(2)	380(60)	0.65(3)	= f3
Fourth moment [$(km/s)^4$]				
f9 = F40	16.114(3)	16000(2000)	0.72(2)	= f4
f10 = F6	16.684(3)	16000(2000)	0.84(2)	= f5
f11 = F7	0.358(4)	12000(2000)	0.09(2)	= f1
FPF method [km/s]				

Acknowledgments

I would like to thank both my supervisors, Conny and Konstanze, for everything I have learned with this project and for their advice to make me improve as a scientist. Specially Konstanze for her constant help, moral support and positive energy even when I know that it was not an easy year for her. Thank you for the very productive but always fun skype meetings and for those encouraging emails that arrived always in the best moments.

Apart from them, it is important to me to thank those who, even when their names are not in the front page of this report, were crucial for its development. I am really thankful to Andrew for his constant guidance and advice as one more of my supervisors. Also to Timothy, Péter, Valentina and Jonas for their kind help always that I needed it and the useful discussions about my target.

Last but not least, I want to thank all my colleagues for every single crazy moment during these two years.

Bibliography

Aerts, C. 1996, A&A, 314, 115

Aerts, C., Christensen-Dalsgaard, J., & Kurtz, D. W. 2010, Asteroseismology

Aerts, C., de Pauw, M., & Waelkens, C. 1992, A&A, 266, 294

Antoci, V., Handler, G., Campante, T. L., et al. 2011, Nature, 477, 570

Antoci, V., Cunha, M., Houdek, G., et al. 2014, ApJ, 796, 118

Asplund, M., Grevesse, N., Sauval, A. J., & Scott, P. 2009, ARA&A, 47, 481

Auvergne, M., Bodin, P., Boisnard, L., et al. 2009, A&A, 506, 411

Balona, L. A., Catanzaro, G., Abedigamba, O. P., Ripepi, V., & Smalley, B. 2015, MNRAS, 448, 1378

Balona, L. A., & Dziembowski, W. A. 2011, MNRAS, 417, 591

Baudin, F., Baglin, A., Orcesi, J.-L., et al. 2006, in ESA Special Publication, Vol. 1306, ESA Special Publication, ed. M. Fridlund, A. Baglin, J. Lochard, & L. Conroy, 145

Boisnard, L., & Auvergne, M. 2006, in ESA Special Publication, Vol. 1306, ESA Special Publication, ed. M. Fridlund, A. Baglin, J. Lochard, & L. Conroy, 19

Bowman, D. M., & Kurtz, D. W. 2014, MNRAS, 444, 1909

Breger, M., Lenz, P., & Pamyatnykh, A. A. 2009, MNRAS, 396, 291

Breger, M., Stich, J., Garrido, R., et al. 1993, A&A, 271, 482

Breger, M., Balona, L., Lenz, P., et al. 2011, MNRAS, 414, 1721

Christensen-Dalsgaard, J. 2000, in Astronomical Society of the Pacific Conference Series, Vol. 210, Delta Scuti and Related Stars, ed. M. Breger & M. Montgomery, 187

Dupret, M.-A., Grigahcène, A., Garrido, R., et al. 2005, MNRAS, 361, 476

Eddington, A. S. 1926, The Internal Constitution of the Stars

García Hernández, A., Moya, A., Michel, E., et al. 2009, A&A, 506, 79

—. 2013, A&A, 559, A63

Gilliland, R. L. 1995, in Astronomical Society of the Pacific Conference Series, Vol. 76, GONG 1994. Helio- and Astro-Seismology from the Earth and Space, ed. R. K. Ulrich, E. J. Rhodes, Jr., & W. Dappen, 578

Gontcharov, G. A. 2006, Astronomy Letters, 32, 759

Grenier, S., Baylac, M.-O., Rolland, L., et al. 1999, A&AS, 137, 451

Guenther, D. B., & Brown, K. I. T. 2004, ApJ, 600, 419

Guenther, D. B., Demarque, P., Kim, Y.-C., & Pinsonneault, M. H. 1992, ApJ, 387, 372

Hansen, C. J., & Kawaler, S. D. 1994, Stellar Interiors. Physical Principles, Structure, and Evolution.

Høg, E., Fabricius, C., Makarov, V. V., et al. 2000, A&A, 355, L27

Iglesias, C. A., & Rogers, F. J. 1996, ApJ, 464, 943

Kaufer, A., & Pasquini, L. 1998, in Society of Photo-Optical Instrumentation Engineers (SPIE) Conference Series, Vol. 3355, Optical Astronomical Instrumentation, ed. S. D'Odorico, 844–854

Kippenhahn, R., & Weigert, A. 1990, Stellar Structure and Evolution

Koch, D. G., Borucki, W. J., Basri, G., et al. 2010, ApJL, 713, L79

Kochukhov, O. 2004, A&A, 423, 613

Kochukhov, O. 2011, in IAU Symposium, Vol. 273, IAU Symposium, ed. D. Prasad Choudhary & K. G. Strassmeier, 249–255

Kolbas, V., Pavlovski, K., Southworth, J., et al. 2015, ArXiv e-prints, arXiv:1506.01254

Kurtz, D. W. 1992, MNRAS, 259, 701

Kurtz, D. W., Saio, H., Takata, M., et al. 2014, MNRAS, 444, 102

Kurtz, D. W., Shibahashi, H., Murphy, S. J., Bedding, T. R., & Bowman, D. M. 2015, MNRAS, 450, 3015

Lampens, P., Tkachenko, A., Lehmann, H., et al. 2013, A&A, 549, A104

Lehmann, H., Tsymbal, V., Mkrtichian, D. E., & Fraga, L. 2006, A&A, 457, 1033

Lenz, P., & Breger, M. 2005, Communications in Asteroseismology, 146, 53

Lovis, C., Pepe, F., Bouchy, F., et al. 2006, in Society of Photo-Optical Instrumentation Engineers (SPIE) Conference Series, Vol. 6269, Society of Photo-Optical Instrumentation Engineers (SPIE) Conference Series, 0

Mantegazza, L. 2000, in Astronomical Society of the Pacific Conference Series, Vol. 210, Delta Scuti and Related Stars, ed. M. Breger & M. Montgomery, 138

Mantegazza, L., Poretti, E., Michel, E., et al. 2012, A&A, 542, A24

Matthews, J. M. 2007, Communications in Asteroseismology, 150, 333

Pamyatnykh, A. A. 2000, in Astronomical Society of the Pacific Conference Series, Vol. 210, Delta Scuti and Related Stars, ed. M. Breger & M. Montgomery, 215

Papics, P. I. 2013, PhD thesis, Instituut voor Sterrenkunde, KU Leuven, Belgium

Pápics, P. I., Briquet, M., Baglin, A., et al. 2012, A&A, 542, A55

Petersen, J. O. 1973, ApJ, 27, 89

—. 1978, ApJ, 62, 205

Poretti, E., Rainer, M., Mantegazza, L., et al. 2013, in Astrophysics and Space Science Proceedings, Vol. 31, Stellar Pulsations: Impact of New Instrumentation and New Insights, ed. J. C. Suárez, R. Garrido, L. A. Balona, & J. Christensen-Dalsgaard, 39

Poretti, E., Alonso, R., Amado, P. J., et al. 2005, AJ, 129, 2461

Poretti, E., Michel, E., Garrido, R., et al. 2009, A&A, 506, 85

Rodríguez, E., & Breger, M. 2001, A&A, 366, 178

Saio, H., Kurtz, D. W., Takata, M., et al. 2015, MNRAS, 447, 3264

Schmid, V. S., Themessl, N., Breger, M., et al. 2012, Astronomische Nachrichten, 333, 1080

Schrijvers, C., Telting, J. H., Aerts, C., Ruymaekers, E., & Henrichs, H. F. 1997, A&AS, 121, 343

Shulyak, D., Tsymbal, V., Ryabchikova, T., Stütz, C., & Weiss, W. W. 2004, A&A, 428, 993

Stellingwerf, R. F. 1978, ApJ, 224, 953

Tkachenko, A., Lehmann, H., Smalley, B., Debosscher, J., & Aerts, C. 2012, MNRAS, 422, 2960

Tkachenko, A., Van Reeth, T., Tsymbal, V., et al. 2013, A&A, 560, A37

Tsymbal, V. 1996, in Astronomical Society of the Pacific Conference Series, Vol. 108, M.A.S.S., Model Atmospheres and Spectrum Synthesis, ed. S. J. Adelman, F. Kupka, & W. W. Weiss, 198

Uytterhoeven, K., Moya, A., Grigahcène, A., et al. 2011, A&A, 534, A125

van Leeuwen, F. 2007, A&A, 474, 653

Walker, G., Matthews, J., Kuschnig, R., et al. 2003, PASP, 115, 1023

Wenger, M., Ochsenbein, F., Egret, D., et al. 2000, A&AS, 143, 9

Zima, W. 2006, A&A, 455, 227

—. 2008, Communications in Asteroseismology, 155, 17

Zima, W., Lehmann, H., Stütz, C., Ilyin, I. V., & Breger, M. 2007, A&A, 471, 237

Zwintz, K., Lenz, P., Breger, M., et al. 2011, A&A, 533, A133

Zwintz, K., Fossati, L., Ryabchikova, T., et al. 2014, Science, 345, 550

Instituut voor Sterrenkunde
Celestijnenlaan 200D BUS 2401
3001 LEUVEN, BELGIË
tel. + 32 16 32 70 27
fax + 32 16 32 79 99
www.kuleuven.be